Palaeogeography, Palaeoclimatology, Palaeoecology 526 (2019) 96–109

Contents lists available at ScienceDirect

Palaeogeography, Palaeoclimatology, Palaeoecology

journal homepage: www.elsevier.com/locate/palaeo

Cyclic late Katian through Hirnantian glacioeustasy and its control of the development of the organic-rich Wufeng and Longmaxi shales, South China

Yangbo Lu[a,c], Chunju Huang[b,*], Shu Jiang[c,d,**], Jingyu Zhang[a], Yongchao Lu[a,c], Yang Liu[b]

[a] Institute of Earth Resources, China University of Geosciences, Wuhan, Hubei 430074, China
[b] State Key Laboratory of Biogeology and Environmental Geology, School of Earth Sciences, China University of Geosciences, Wuhan 430074, China
[c] Key Laboratory of Tectonics and Petroleum Resources, Ministry of Education, China University of Geosciences, Wuhan, Hubei 430074, China
[d] Energy and Geoscience Institute (EGI), University of Utah, Salt Lake City, UT 84108, United States of America

ARTICLE INFO

Keywords:
Astronomical forcing
Condensed section
Sea-level fluctuations
Time series analysis
Hirnantian glaciation
Organic matter enrichment

ABSTRACT

Deposition of the organic-rich shales of the Wufeng and lowermost Longmaxi formations (late Katian through Hirnantian) occurred in a relatively stable tectonic setting and commenced at approximately 4.5 Myr prior to the end-Ordovician glacial maximum. These organic-rich shales are important because they provide a continuous sedimentary record of high-frequency eustatic changes associated with ice-sheet expansion and shrinkage. Here, we carried out a high-resolution cyclostratigraphic study of Fe^{3+} series and associated geochemical analysis of the Wufeng and lowermost Longmaxi shales in order to better understand sea-level cyclicity in the late Katian through Hirnantian ocean. The organic-rich shales deposited during this interval in the EHD1 drill core (Yichang, China) record four major Myr-scale eustatic cycles, which were associated with third-order sea-level fluctuations. Within each of these major cycles, 3–4 minor eustatic cycles corresponding to 405-kyr long eccentricity astronomical cycles were recognized and representing fourth-order eustatic changes. The cyclostratigraphic age of this study is generally in agreement with the radiometric dates in GTS2012, although the duration of the Hirnantian stage is ~0.5 Myr longer than previously thought. This study also infers glacial controls on the depositional environment of the organic-rich shales, as enhanced cooling triggered ice-sheet expansion and concurrent sea-level fall, leading to higher thermohaline circulation intensity and enhanced paleoproductivity through upwelling and terrestrial influx. In contrast, warming intervals led to ice-sheet shrinkage and concurrent deepening characterized by water column stratification and reduced nutrient supply. The results provide evidence in support of continuous continental glaciation in the late Katian through Hirnantian.

1. Introduction

The organic-rich marine black shale of the Upper Ordovician Wufeng Formation and the lowermost Longmaxi Formation (late Katian through Hirnantian) are widely developed in the Upper Yangtze area, South China. They were deposited during the Ordovician-Silurian (O-S) transition during which continuous global cooling of the Late Ordovician culminated in a short but intense glaciation in the Hirnantian, the final stage of the Ordovician (Algeo et al., 2016). In the course of this glaciation, a massive ice-sheet was widespread on the supercontinent of Gondwana near the Paleo-South Pole (Brenchley et al., 1994; Chen et al., 2006; Delabroye and Vecoli, 2010; Finnegan et al., 2011; Elrick et al., 2013). Although no unambiguous glacial record of the Late Ordovician age has yet been found prior to the Hirnantian, several authors have suggested pre-Hirnantian ice-sheet development based on various approaches including paleoecology (Ainsaar et al., 2004; Bourahrouh et al., 2004; Achab and Paris, 2007; Ghavidel-Syooki, 2017), sedimentary petrology (Loi, 1993; Loi et al., 2010; Lavoie, 1995; Hamoumi, 1999), paleoceanography (Pope and Read, 1998; Pope and Steffen, 2003) and isotopic proxies (Ainsaar et al., 1999; Saltzman and Young, 2005; Finnegan et al., 2011).

Due to gravitational planetary motions and their mutual interactions, quasi-periodic oscillations in Earth's orbital parameters (eccentricity, obliquity, and precession) have driven climatic and sea-level changes via variations in the intensity of solar radiation (insolation) reaching the Earth's surface. These orbital cycles are frequently recorded in climate-sensitive proxies within sedimentary archives of Earth history (e.g., Imbrie et al., 1984; Strasser et al., 2006; Boulila

* Corresponding author.
** Correspondence to: S. Jiang, Key Laboratory of Tectonics and Petroleum Resources, Ministry of Education, China University of Geosciences, Wuhan, Hubei 430074, China.
E-mail addresses: huangcj@cug.edu.cn (C. Huang), jiangsu@cug.edu.cn (S. Jiang).

https://doi.org/10.1016/j.palaeo.2019.04.012
Received 13 December 2018; Received in revised form 11 April 2019; Accepted 11 April 2019
Available online 15 April 2019
0031-0182/ © 2019 Elsevier B.V. All rights reserved.

et al., 2011). Such cycles can drive ice-sheet expansion and shrinkage, leading to orbitally controlled glacioeustatic changes. Such a control has been invoked for the Late Ordovician (e.g., Williams, 1991; Sutcliffe et al., 2000; Long, 2007; Loi et al., 2010; Elrick et al., 2013; Svensen et al., 2015; Fang et al., 2016; Hinnov and Diecchio, 2016; Huang et al., 2016). The Wufeng Formation and the lowermost Longmaxi Formation in the Upper Yangtze area contain a continuous sedimentary record of organic-rich shale deposited in deep shelf (intra-shelf) low setting (Lu et al., 2017), which provides an opportunity to examine the evidence of astronomical forcing and glacioeustasy in the late Katian through Hirnantian in a low-latitude region. Moreover, they also allow for insights into climatic dynamics in the subtropics during an important greenhouse to icehouse transition. In this study, a cyclostratigraphic analysis of Fe^{3+} series of the Wufeng Formation and the lowermost Longmaxi Formation was carried out. The main objectives of this paper are: (1) seek evidence for astronomical signals and establish a floating astronomical time scale (ATS) for the late Katian through Hirnantian; (2) evaluate the possible interrelation between astronomical cycles and contemporaneous eustatic changes; (3) examine the orbitally-forced climate changes and their effects on the accumulation of organic-rich shales.

2. Geological setting

During the Middle Ordovician (~460 Ma), the Nanhua Basin (a failed intracontinental rift basin) between the Yangtze Block and the Cathaysia Block began to close, resulted in a united South China Block (SCB) (Wang, 1985). The Upper Yangtze area was part of the SCB, and it was located close to the paleo-equator during the Late Ordovician, along the northwestern margin of Gondwana (Metcalfe, 1994; Huang et al., 2018) (Fig. 1A) (note: SCB was rotated ~90° counter-clockwise relative to its modern position as shown in Fig. 1B). In the late Katian (~448 Ma), the Upper Yangtze area was a large depression bounded by surrounding hinterland and tectonic uplifts, and in communication with the Qinling Ocean through relatively narrow straits (Chen et al., 2004, 2013; Liu et al., 2017). It was tectonically stable until the development of the Yichang Uplift that was driven by the Kwangsian (Caledonian) Orogeny, forming a diachronous stratigraphical break between the Rhuddanian and Aeronian (Chen et al., 2014). Covered by a broad epicontinental sea, the Upper Yangtze area was an enclosed, semi-restricted and low-energy sea characterized by anoxic bottom waters prior to the Hirnantian glacial event (Chen et al., 2004; Yan et al., 2009). It was under these conditions that a thin (~8 to 12 m in total thickness) set of organic-rich siliceous mudstone, was deposited. The upper Katian through Hirnantian Wufeng Formation contains well-preserved graptolite fossils, and it is in unconformable contact with the underlying nodular calcareous limestone or sandstone of the Upper Ordovician Linxiang Formation (also called the Jiancaogou Formation). The Hirnantian Guanyinqiao Bed overlies the Wufeng Formation, and is mainly composed of a thin layer (< 0.5 m) of calcareous mudstone or limestone that contains the Hirnantia Fauna, a cool-water shelly fauna that spread rapidly at the onset of the Hirnantian glaciation and disappeared abruptly at its termination (Rong et al., 2002; Zhan et al., 2010). The Guanyinqiao Bed was deposited under oxic conditions and has been interpreted to represent the interval when sea level was at its lowest during the peak of the Hirnantian glacial maximum (Fan et al., 2009). The Longmaxi Formation, which conformably overlies the Guanyinqiao Bed, consists of > 50 m of dark gray to black silty shale that was deposited in the late Hirnantian through Rhuddanian.

The EHD1 borehole (30°06′08″ N, 110°0813″ E) was drilled by Oil and Gas Resources Investigation Center of China Geological Survey (Fig. 1B). The drilling was targeted for preliminary assessment of the shale gas exploration and development in the Ordovician-Silurian Wufeng-Longmaxi formations, and the Cambrian Niutitang Formation. The borehole is located at approximately 120 km northwest of the Wangjiawan section (30°58′56″ N and 111°25′10″ E), which is the Global Stratotype Section and Point (GSSP) for the base of the Hirnantian Stage (Fig. 1B). Graptolite biozonation is well established in the Wangjiawan section (Chen et al., 2006, 2017) and each biozone has an assigned isotopic age (Gradstein et al., 2012). Despite the surrounding paleo-uplifts and submarine highs, the facies patterns are generally consistent throughout the Upper Yangtze area (Chen et al., 2004). Recent studies also made intriguing attempts to integrate the sequence stratigraphy and biostratigraphy across the Upper Yangtze area (Lu et al., 2017; Chen et al., 2018). The top surfaces of black calcareous mudstone were interpreted as the transgressive deepening events with the arrival of new graptolite assemblages (Fig. 2). This interpretation is supported by rising natural gamma-ray (GR) values that correspond to high sea level, and the first appearance of datum (FAD) of the successive graptolite biozones that were identified (Fig. 2). A regional correlation was established between the Wangjiawan section, EHD1 borehole and Jiaoye1 borehole, with Guanyinqiao Bed as the marker bed (Fig. 3). The 8.1-m-thick Wufeng Formation penetrated by the EHD1 borehole covers the *Dicellograptus complanatus* (abbreviated as WF1), *Dicellograptus complexus* (WF2), *Paraorthograptus pacificus* (WF3), and *Normalograptus extraordinarius* (WF4) graptolite subzones in ascending order. The Guanyinqiao Bed in EHD1 borehole is ~20 cm in thickness. The overlying lowermost part of the Longmaxi Formation is ~1 m thick. It was deposited in the late Hirnantian and dominated by *Persculptograptus persculptus* (LM1). The Katian/Hirnantian and Ordovician/Silurian boundaries were determined via a comprehensive consideration of the FAD identification of WF4 and *Akidograptus ascensus* (LM2), and the GR profile. Based on the estimation through a constrained optimization (CONOP) method, the combined duration of the studied interval is ~4.55 Myr (from 448.38 Ma to 443.83 Ma) (Gradstein et al., 2012; Chen et al., 2017).

3. Data and methods

3.1. High-resolution imaging and data selection

The upper Katian through Hirnantian organic-rich shales span an interval from 487.45 to 496.55 m in the EHD1 borehole, and they were selected for cyclostratigraphic analysis (Fig. 2). After coring, the entire fresh core of EHD1 borehole was scanned using a CSIRO-developed HyLogging™ system. Hyperspectral data of minerals and high-resolution images were obtained using a HyLogger-1 scanner that was adapted to take spectral measurements every 1.0 cm along with the drill core. Continuous digital core imagery settings followed the HyLogger configurations proposed by Schodlok et al. (2016). Before scanning, the drill core was completely dried and cleaned of surface contamination. In the scanning mode, the instrument acquired visible–near-infrared (VNIR 400–1100 nm) and short wavelength infrared (SWIR 1100–2500 nm) reflectance spectra. Automatic processing and interpretation of the raw data were undertaken using The Spectral Geologist™ (TSG) software, as well as spectral interpretation methods and spectral libraries developed by AusSpec. All spectral interpretations were verified using in-house methods to determine the best mineral mix match for each spectrum (Schodlok et al., 2016). The scanning was performed at the Sichuan Coal Field Geological Engineering Survey and Design Institute in Shennongjia, Hubei province.

High-resolution imaging using the HyLogging system provides the concentration of various minerals and elements including quartz, labradorite, kaolinite, illite, muscovite, montmorillonite, chlorite, hornblende, calcite, dolomite, gypsum and iron oxide (Fe^{3+}). Amongst these, iron concentration in sedimentary rocks is stable, i.e., it is not significantly influenced by post-burial diagenetic alteration (Westerhold et al., 2007, 2008). Fe^{3+} (oxides) bearing minerals reflect the amount of terrigenous material in the sediment (Westerhold et al., 2007, 2008). Herein, the Fe^{3+} concentration inferred from the 565 nm peaks in the VNIR spectrum shows a significantly higher signal-to-noise ratio than other physical property measurements (e.g., GR log, color

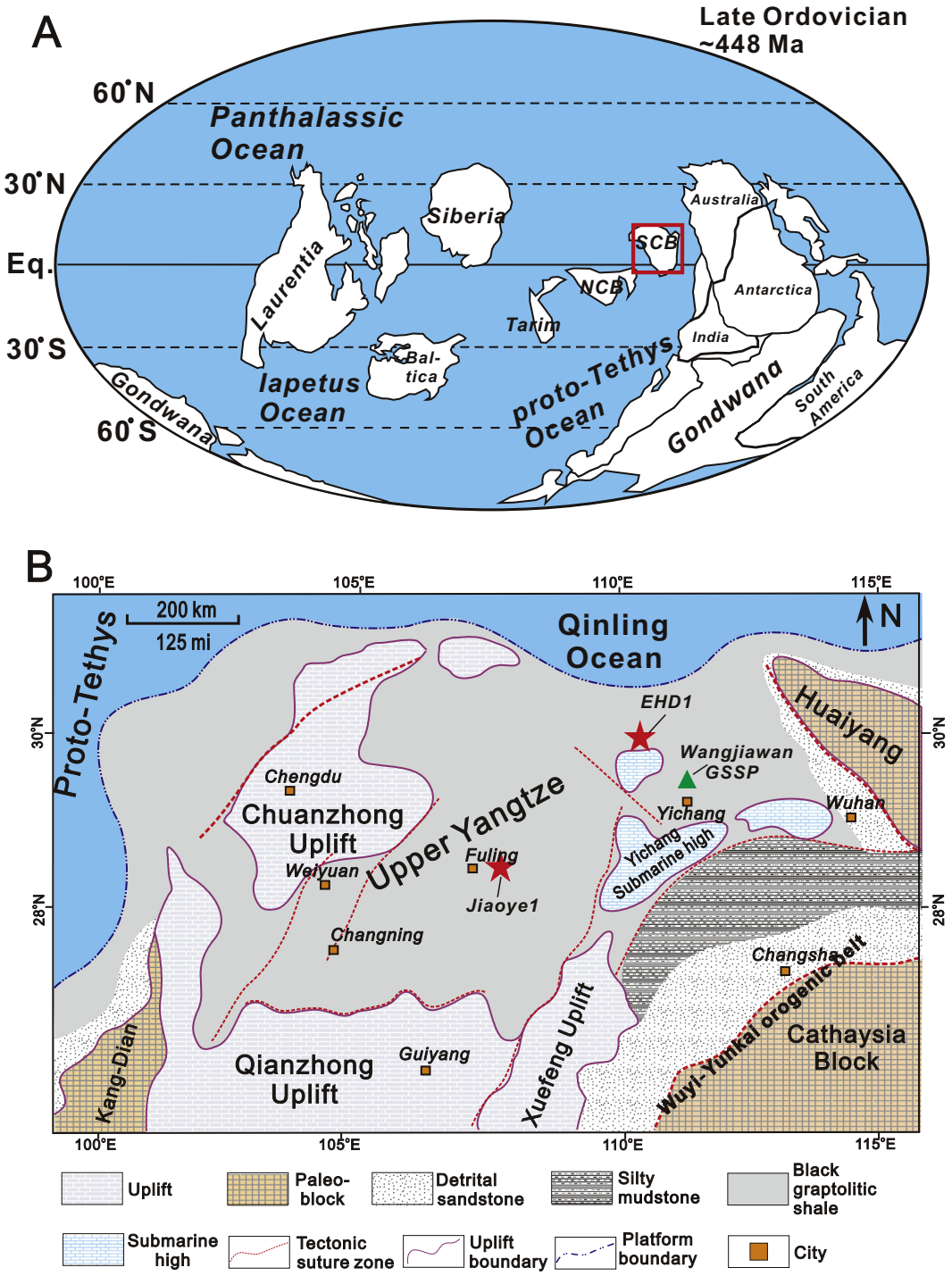

Fig. 1. A. Paleogeographic map of the Upper Yangtze area during the Late Ordovician (~448 Ma) showing the location of the study area (after Metcalfe, 1994; Huang et al., 2018). SCB = South China Block; NCB = North China Block. Note that SCB was rotated ~90° counter-clockwise relative to its modern orientation, and it represents only one of many models for the Ordovician plate reconstruction. B. Geological map showing the modern location of SCB and localities of the EHD1 borehole, Jiaoye1 borehole and Wangjiawan section (after Lu et al., 2017).

reflectance). Therefore, it was considered reliable and chosen to conduct fundamental cyclostratigraphic analyses in this study.

3.2. X-ray fluorescence (XRF) measurements

X-ray fluorescence (XRF) data was measured through the studied interval at ~10 cm intervals using a handheld energy dispersive XRF spectrometer (Niton XL2) with 60-second recording time. A total of 16 layers of K-bentonites were identified in the core, and these were avoided in order to exclude the irregular signals attributable to volcanic influence. The X-ray beam from the Niton XL2 covers an area of ~2 cm^2 (1.4 × 1.4 cm). X-ray absorption spectra were recorded in scanning mode from 3 to 40 keV, and the absorption peaks were analyzed using "soil mode" in proprietary Innov-X software. The precision of handheld XRF data generally increases with increasing measurement time. The 60 s testing time adopted in this study ensures adequate data for elements with concentrations between 20 and 30 ppm (Dahl et al., 2013).

The XRF measurements were recorded as the counts per second

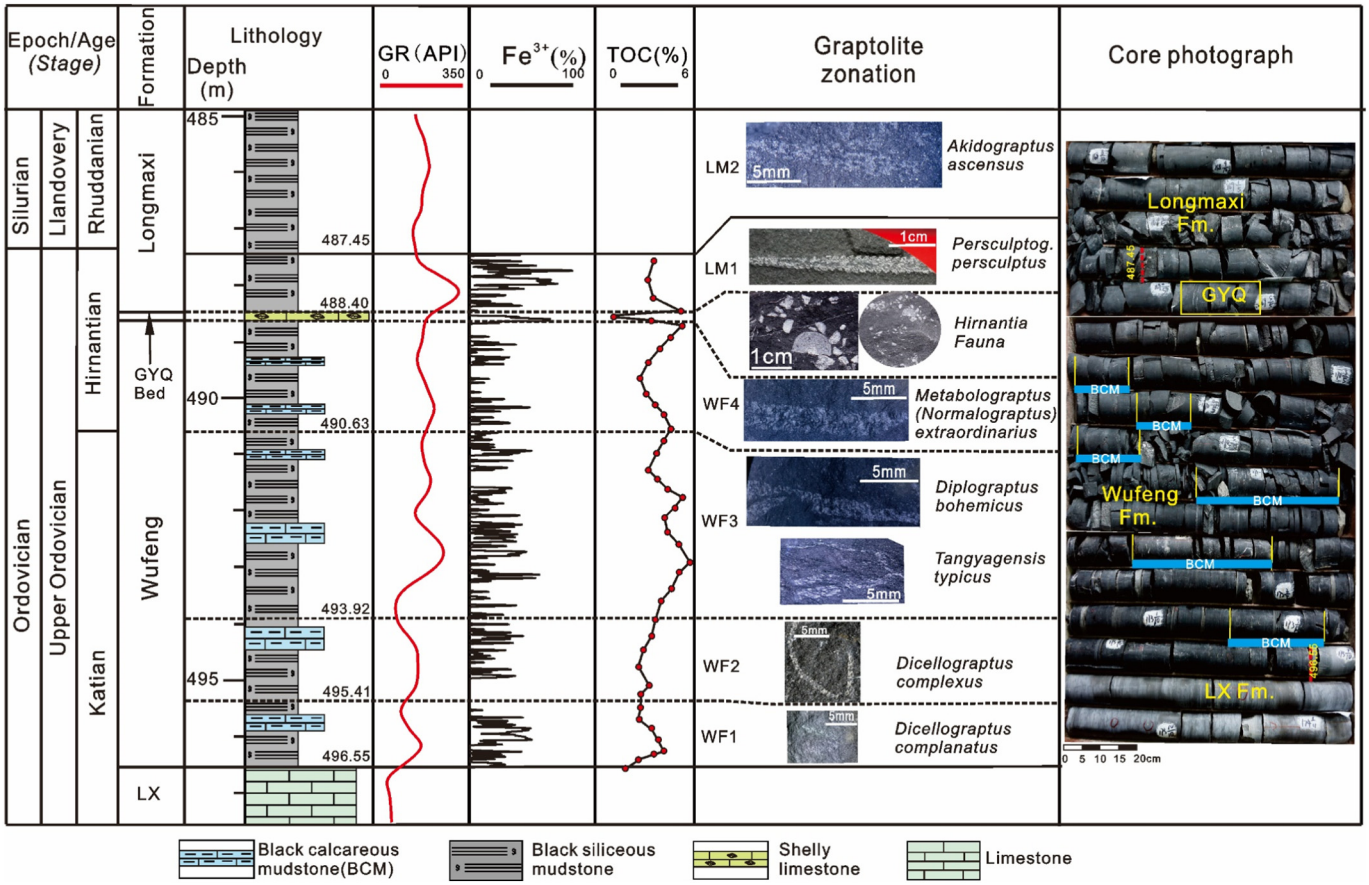

Fig. 2. Chronostratigraphy and lithostratigraphy of the studied interval in the EHD1 borehole, and core photograph indicating the boundaries between formations. GYQ Bed = Guanyinqiao Bed; GR = gamma-ray; TOC = total organic carbon; LX = Linxiang. Graptolite zones including *Dicellograptus complanatus* (WF1), *Dicellograptus complexus* (WF2), *Paraorthograptus pacificus* (WF3), *Normalograptus extraordinarius* (WF4) and *Persculptograptus persculptus* (LM1).

(cps) values and were automatically converted into parts per million (ppm) by the Niton instrument. Elements including titanium (Ti), magnesium (Mg), copper (Cu), nickel (Ni), vanadium (V) and chromium (Cr) were assessed in our paleoclimate analyses, and the average values of the selected elements exceed the nominal sensitivity (refer to light elements not visible to XRF) of the instrument (3873.7, 6328.5, 144.3, 701.3, 1261.4 and 264.4 ppm for Ti, Cu, Ni, V, and Cr, respectively).

3.3. Total organic carbon (TOC)

Forty-three fresh rock samples of core material were collected at ~0.2 m intervals through the studied interval. These were pulverized to finer than 200-mesh size using a Retsch vibratory disc mill. TOC analyses were carried out in the Key Laboratory of Tectonics and Petroleum Resources, China University of Geosciences (Wuhan). About 200 mg of powder was weighted and treated with 10% HCl acid at 60 °C to remove carbonate, and then washed with distilled water to remove remaining HCl. The residue was dried and analyzed on a Leco CS-200 elemental analyzer. The analytical precision of the TOC measurements was better than 0.5%, based on replicate analyses of the Chinese national standard GB/T 19145-2003 (Zeng et al., 2013).

The TOC content of the organic-rich shales ranges from 0.6% to 5.8% with an average of 3.6% (Fig. 2). The interval with lowest TOC (0.5%) content corresponds to the shelly limestone of the Guanyinqiao Bed (core depth of 488.40–488.60 m), and the highest TOC content is at a core depth of ~492.9 m. The TOC profile also bears close similarity with the GR profile, i.e., the sections with higher TOC content generally display higher GR values. This is expected since uranium, thorium, and potassium are typically enriched in sediments high in organic matter (OM).

3.4. Time-series analysis methods

The Fe^{3+} series derived from the HyLogging data were analyzed with the multitaper method (MTM) spectral estimator (Thomson, 1982) using the SSA-MTM Toolkit (Ghil et al., 2002). Peaks in the spectra that may represent astronomical cyclicity were tested against robust red noise models fitted to the gross morphology of the spectra at the 85%, 90%, 95% and 99% confidence levels (Mann and Lees, 1996). Gaussian filtering and amplitude spectrum analysis were implemented in AnalySeries 2.0.8 software (Paillard et al., 1996). Short orbital eccentricity and precession cycles were modulated by long orbital eccentricity (Laskar et al., 2004). “Age Scale” function was used in AnalySeries software for Fe^{3+} series tuning. The interpreted 405-kyr long-eccentricity cycles were extracted using Gaussian bandpass filters and were tuned to an artificial sinusoidal age model to establish a floating ATS. The correlation coefficient (COCO) was performed in Acycle0.26 software to evaluate the significance level of the null hypothesis of no orbital forcing (Li et al., 2018). The sedimentation rate was examined through the evolutionary correlation coefficient (eCOCO) function (Li et al., 2018). The GR, TOC and geochemical series of depth domain were converted to the time domain using the 405-kyr picks of the Fe^{3+} series.

3.5. Late Ordovician orbital parameters

Although many authors have made attempts to quantify the periods

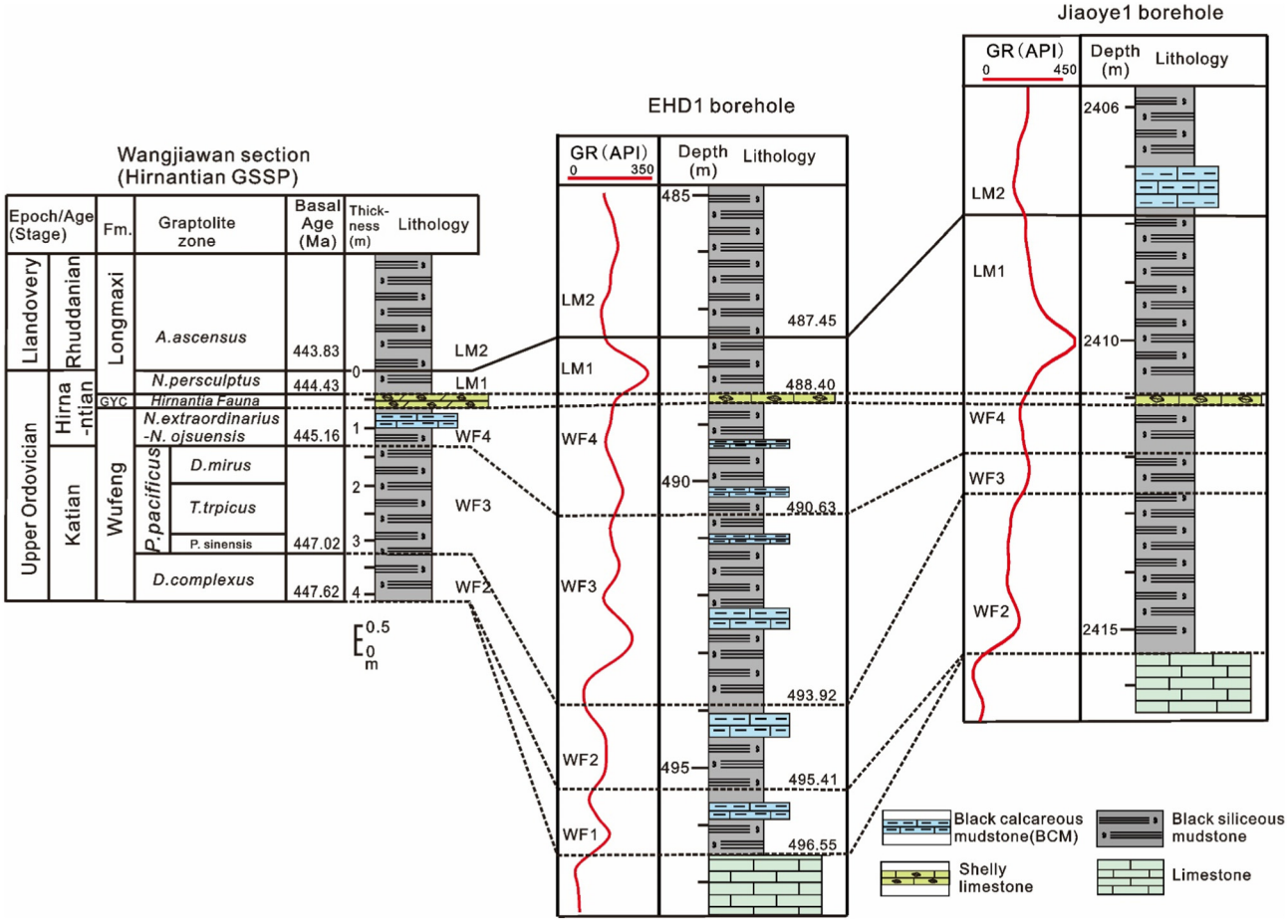

Fig. 3. Regional stratigraphic correlation between the Wangjiawan section, EHD1 borehole and Jiaoye1 borehole. GSSP = Global Stratotype Section and Point; GYQ = Guanyinqiao Bed; WF1 = *Dicellograptus complanatus*, WF2 = *Dicellograptus complexus*, WF3 = *Paraorthograptus pacificus*, WF4 = *Normalograptus extraordinarius*, LM1 = *Persculptograptus persculptus* and LM2 = *Akidograptus ascensus* (the Wangjiawan section was after Yan et al., 2009; Chen et al., 2006. The Jiaoye1 borehole was after Chen et al., 2018).

of astronomical parameters (eccentricity, obliquity, and precession) in the Paleozoic (e.g. Wu et al., 2013; Svensen et al., 2015; Fang et al., 2016; Pas et al., 2018; Zhong et al., 2018), a full astronomical solution for the early Paleozoic has not yet been established. Nevertheless, it is believed that 405-kyr long-eccentricity cycles remained consistent throughout Earth history, owing primarily to the stable orbit of Jupiter (Laskar et al., 2004). Short eccentricity is also expected with several components ranging from 95 to 131 kyr (Berger et al., 1992; Berger and Loutre, 1994; Laskar et al., 2004). With regard to the periods of obliquity and precession, several models proposed inconsistent cycle durations for the Ordovician. With the assumption of constant moon-recession rate, Berger and Loutre (1994) suggested 37.3 kyr and 30.6 kyr for obliquity, and 19.3 kyr and 16.4 kyr for precession. The La 2004 model (Laskar et al., 2004) indicated the main obliquity period of 25.6 kyr and precession periods of 18.1 kyr, 17.4 kyr, and 15.5 kyr under the influence of tidal time lag (Laskar et al., 2004). The former two models may result in over or under-estimation of the periods in the Paleozoic era (Waltham, 2015; Zhong et al., 2018). Therefore, the latest estimates from Waltham (2015) were adopted in this study. Waltham (2015) calculated periods of 33.1 ± 3.9 kyr for short (main) obliquity, and 20.8 ± 1.5 kyr, 19.8 ± 1.3 kyr, 17.1 ± 1.0 kyr, and 17.2 ± 1.0 kyr for precession. The ratios of periodicities of the orbital parameters were 405: 125: 95: 33.3: 20.8: 19.8: 17.1. In addition, several studies demonstrated the existence of grand cycles associated with eccentricity (~2.4 Myr) or obliquity (~1.2 Myr) in the Ordovician period (Loi et al., 2010; Crampton et al., 2018; Zhong et al., 2018), therefore, the presence of grand orbital cycles are expected in the astronomical analysis.

4. Results

4.1. Spectral analysis

The MTM power spectrum of the Fe^{3+} series shows a hierarchy of cycles throughout the studied interval with periodicities at ~2.2 m and ~0.75 m above 99% confidence level (CL). There are also significant peaks of 0.37–0.23 m above 95% CL, and other peaks of 0.067–0.055 m and ~0.042–0.037 m above 95% CL (Fig. 4B). Based on the expected ratios of the Late Ordovician astronomical parameters, coupled with the existing time constraints on the studied interval biostratigraphy (Gradstein et al., 2012), the wavelengths of the ~0.75 m cycles were provisionally interpreted as the 405-kyr long-eccentricity cycles. Hence, the sedimentary cycles of ~2.2 m, 0.37–0.23 m, and 0.067–0.055 m and 0.042–0.037 m may correspond to ~1.2-Myr long obliquity, ~125–95-kyr short eccentricity, ~33.3-kyr short obliquity, and ~20.8–17.1-kyr precession, respectively. This interpretation is compatible with the further observation that each 0.75 m (~405-kyr) cycle is composed of approximately three smaller short-eccentricity (~125–95-kyr) cycles (Fig. 4A).

4.2. Astronomical tuning

The putative 405-kyr long-eccentricity cycles were used as a tuning target to establish a high-resolution age model. The power spectrum of

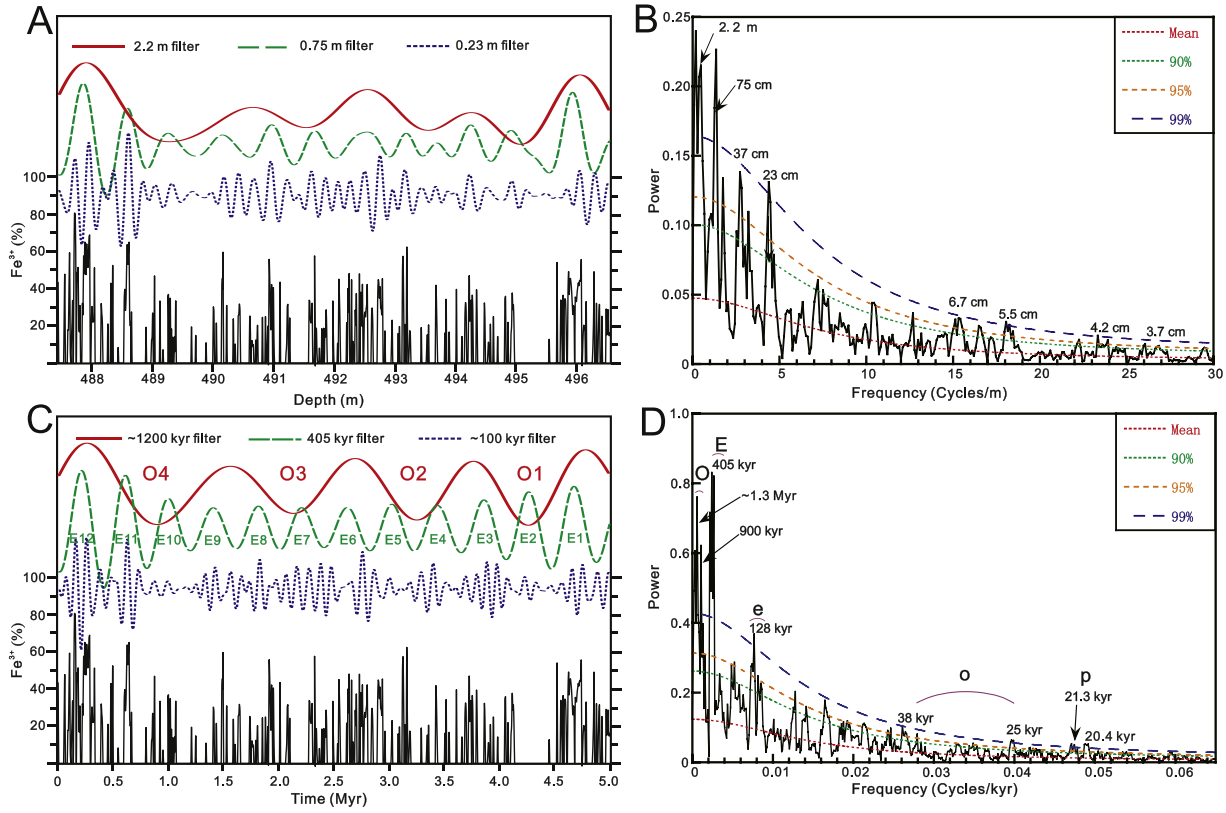

Fig. 4. A. Interpreted astronomical components of the Fe^{3+} series based on spectral analysis. Fe^{3+} data and astronomical components in the depth domain. Astronomical components were extracted with Gaussian bandpass filters in the depth domain. B. 2π MTM (multitaper method) power spectra of Fe^{3+} series in the depth domain. Significant peaks are labeled in meters; results of robust noise modeling are shown: mean is the median smoothed, fitted red noise spectrum; the upper 90%, 95%, and 99% confidence levels are also shown. C. Interpreted astronomical components of Fe^{3+} series were extracted with Gaussian bandpass filters in the time domain. D. MTM power spectrum of the 405-kyr calibrated Fe^{3+} series with significant peaks labeled in kyr (kiloyears). O, E, e, o, and p represent the long obliquity, long eccentricity, short eccentricity, obliquity and precession cycles, respectively. (For interpretation of the references to color in this figure legend, the reader is referred to the web version of this article.)

the 405-kyr-tuned Fe^{3+} series reveals the presence of all astronomical parameters (Fig. 4D). There are three very distinct peaks corresponding to ~1.2-Myr long obliquity, 405-kyr long eccentricity and ~128-kyr short eccentricity (Fig. 4D). As illustrated in Fig. 4C, ~1.2-Myr long obliquity, ~405-kyr and ~100-kyr eccentricity components in the Fe^{3+} tuned time series were extracted by Gaussian bandpass filtering. The outputs indicate about four ~1.2-Myr long-obliquity cycles and twelve 405-kyr long-eccentricity cycles through the studied interval. The 405-kyr long-eccentricity cycles are grouped into bundles of three into each long-obliquity cycle, and about three or four ~100-kyr cycles are further bundled into larger scale (~405-kyr) cycles (Fig. 4C). These results are consistent with the predicted Late Ordovician astronomical periods of Waltham (2015), and further indicate that our astronomical interpretation is convincing.

4.3. Evolutionary correlation coefficient

The 9.1-m-long studied section spanned ~5.0 Myr (approximately twelve 405-kyr cycles from Fig. 4C); therefore, a preliminary estimation of the sedimentation rate was ~0.18 cm/kyr. The estimation of the sedimentation rate was tested with eCOCO. An initial COCO analysis with 2000 Monte Carlo simulations was performed on sedimentation rates from 0 to 3 cm/kyr. Three peaks at 0.19 cm/kyr, 0.66 cm/kyr and 0.86 cm/kyr emerge in the COCO analysis (Fig. 5A). All three sedimentation rates are showing significance levels lower than 1%. The null hypothesis of no astronomical signal can be rejected at a 99.9% confidence levels at 0.19 cm/kyr and 0.86 cm/kyr (Fig. 5B) with all seven astronomical frequencies contributing (Fig. 5C). In particular, the sedimentation rate at 0.19 cm/kyr is the most reliable as the null hypothesis of no astronomical signal can be rejected at a 99.99% confidence levels (Fig. 5C), and it is in accordant with the sedimentation rate yielded by MTM. The eCOCO analysis of ρ, H_0 and the number of contributing astronomical frequencies can be used to examine the various sedimentation (Fig. 6A, B, C) (Li et al., 2018). The eCOCO analysis of the Fe^{3+} series indicates a relatively high sedimentation rate at the bottom of the Wufeng Formation (~0.66–0.86 cm/kyr), and it gradually decreases down to ~0.19 cm/kyr for 494–492 m interval and maintains low and steady for 492–489 m interval. The highest sedimentation rates are equivalent to the bottom of the Wufeng Formation and Guanyinqiao Bed. The change of sedimentation rate is discontinuous at ~489 m, indicating a dramatic sea level fall in the Hirnantian.

4.4. Paleoclimate proxies

Vanadium-based proxies (V/Cr and V/(V + Ni)) are commonly used to evaluate the redox conditions of depositional environments (Hatch and Leventhal, 1992; Calvert and Pedersen, 1993; Yan et al., 2009; Chen et al., 2016). In particular, V/(V + Ni) increases as oxygen levels in the water column decrease (Calvert and Pedersen, 1993). Values of 0.46 and 0.6 are the boundaries between oxic/dysoxic, dysoxic/anoxic, respectively (Calvert and Pedersen, 1993). For V/Cr, 2 and 4.25 are the boundaries between oxic/dysoxic and dysoxic/anoxic (Jones and Manning, 1994). The V/(V + Ni) and V/Cr data measured by XRF for this study show similar trends. Average V/(V + Ni) and V/Cr values of the studied section are 0.61 and 4.8, respectively, which suggest anoxic

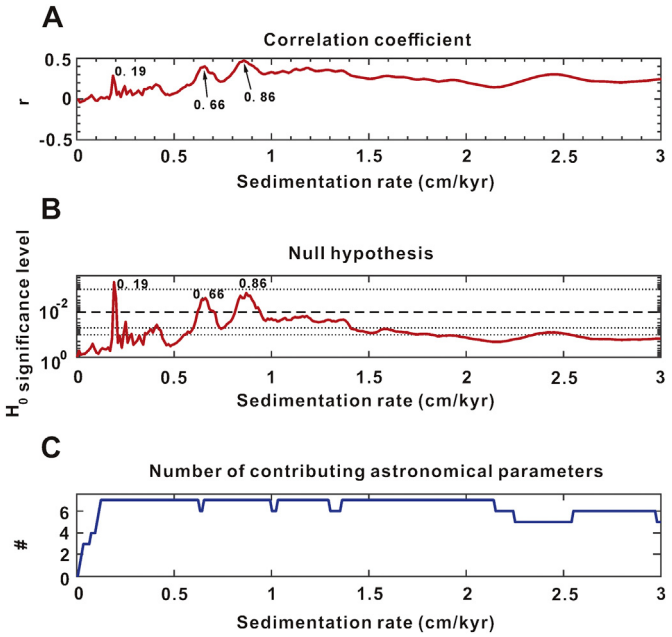

Fig. 5. COCO analysis of the Fe^{3+} series of the EHD1 borehole and target series using Waltham2015 solution at 445 Ma (405: 125: 95: 33.3: 20.8: 19.8: 17.1.) (Waltham, 2015). Sedimentation rates range from 0 to 3 cm/kyr with a step of 0.01 cm/kyr. A. The correlation coefficient spectrum; B. null hypothesis text; C. the number of contributing astronomical frequencies. The number of Monte Carlo (Malinverno et al., 2010) simulation is 2000.

bottom water conditions (Fig. 9). Sustained periodic fluctuations are of a similar pattern in the V/Cr and V/(V + Ni) series, and they appear to match well with the 405-kyr eccentricity pattern interpreted from the Fe^{3+} series, i.e., undulation with a distinctive peak can be observed in every eccentricity cycle (Fig. 9). The 405-kyr cycles filtered output of V/(V + Ni), and V/Cr series show anti-phase relationships with the 405-kyr cycles filtered output of tuned Fe^{3+} series.

Ti is usually bound with clays and continentally derived heavy minerals such as ilmenite and rutile. As such, it is considered an indicator of detrital flux (Rimmer, 2004; Ma et al., 2016). The 405-kyr cycles filtered output of Ti is broadly in-phase with the 405-kyr cycles filtered output of tuned Fe^{3+} series, indicating that increases in terrestrial influx are coeval with oxic conditions during the periods of sea-level fall (Fig. 9). Sea-level fall might lead to the higher terrigenous influx of Fe^{3+} and Ti through enhanced weathering and riverine discharge that resulted from greater exposure of landmass.

In marine sediments, Cu and Ni are readily adsorbed by OM and delivered to the basin mainly in the form of the organometallic complex. These complexes will be retained within the sediment after OM destruction (Nameroff et al., 2004). When normalized to Ti, Cu/Ti and Ni/Ti can provide useful information about changes in paleoproductivity, particularly under anoxic conditions. The profiles of Ni/Ti and Cu/Ti are similar (Fig. 10). Notably, variations in Ni/Ti and Cu/Ti are broadly in phase with the ~1.2-Myr long-obliquity cycles filtered output of tuned Fe^{3+} series (Fig. 10).

Mg concentration indicates a local net magnesium source. Possible sources include the release of magnesium adsorbed to sediment–particle surfaces by ion exchange with pore-fluid NH_4^+, weathering of igneous minerals, and dissolution of carbonates (Higgins and Schrag, 2010). The Mg profile is generally consistent and stable, and not exhibiting any close links to either filtered output of tuned Fe^{3+} series (Fig. 9).

5. Discussion

5.1. Astronomically calibrated chronostratigraphy and biostratigraphy of the late Katian through Hirnantian

In the Geologic Time Scale 2012 (GTS2012; Gradstein et al., 2012), the Ordovician-Silurian time scale was a CONOP fit of global sections with graptolite assemblages (standardized to Australia), followed by spline-fit to selected radio-isotopic ages of 26 radiometrically dated ash beds (with uncertainties of approximately 1 to 3 Myr). In particular, there are only 2 ages for the studied interval: 444.88 ± 1.07 Ma (Tucker et al., 1990) through U-Pb dating in Katian (ca. 4 m below base-Silurian GSSP at Dobbs Linn), and 442.6 ± 5.04 Ma through Ar/Ar dating in the Rhuddanian (Kuiper et al., 2008). The cyclostratigraphic analysis of this study provides an alternative method for precise calibration of the geological time scale. The floating ATS for the studied interval was constructed by tuning the filtered twelve 405-kyr sedimentary cycles to 405-kyr long eccentricity cycles. It was anchored to the O-S boundary and indicating a total duration of ~5.0 Myr. This result is ~0.5 Myr longer than the total duration of ~4.55 Myr assigned by GTS2012 (Fig. 7).

Five complete graptolite zones were identified in the studied interval of the EHD1 borehole, with three in the late Katian and two in the Hirnantian stage. The total thickness of the *Dicellograptus complanatus* (WF1), *Dicellograptus complexus* (WF2), *Paraorthograptus pacificus* (WF3), *Normalograptus extraordinarius* (WF4), and *Persculptograptus persculptus* (LM1) graptolite zones are 1.14 m, 1.49 m, 3.29 m, 2.23 m, and 0.95 m, respectively. According to the floating ATS, the durations of theses graptolite zones are estimated to be 0.63 Myr, 0.82 Myr, 1.80 Myr, 1.22 Myr, and 0.52 Myr for WF1, WF2, WF3, WF4 and LM1 from bottom to top, respectively (Fig. 7). The ~20-cm-thick Guanyinqiao Bed may overlap with both WF4 and LM1 (Chen et al., 2006); therefore, an additional 0.1 Myr uncertainty (corresponding to the deposition interval of ~20 cm) was added to the duration of WF4 and LM1. A ± 0.4 Myr uncertainty was implemented to the stage boundary of the Hirnantian in case of the potential error that there might be overlooked or repetitive counting of a 405-kyr cycle (De Vleeschouwer et al., 2012; Zhong et al., 2018). In comparison, the duration of the WF3 and LM1 zones is in agreement with those of GTS2012 (within 10% deviation). Small differences occur in the WF1 and WF2 zones, where the duration of WF1 and WF2 are ~0.13 Myr shorter and ~0.22 Myr longer than those in GTS2012, but the combined duration of two intervals is similar to the combined duration in GTS2012. The major difference is the duration of WF4 between 1.22 Myr in this study and 0.73 Myr in GTS2012 that caused a longer duration for the Hirnantian stage. Nevertheless, the duration of each biozone is within the duration uncertainties in GTS2012. Therefore, the current CONOP method yields impressively good results. However, considering the significant uncertainty of the radiometric dates, the astronomically calibrated durations of graptolite zones reported in this study should be more reliable.

5.2. Long-period astronomical cycles and third-order eustatic sequence

The stratigraphic record is a composite of superimposed sedimentary cyclicity that can be divided into six orders (Haq and Schutter, 2008). They range from the high-frequency Milankovitch-scale climatic cycles to fourth-order (< 0.5 Myr in duration) and third-order (mostly 1 to 2 Myr in duration) eustatic cycles, and larger tectonic cycles (several million years in duration) (Haq and Schutter, 2008). The origins of third-order eustatic sequences have been long controversial. However, there has been increasing evidence supporting the view that long astronomical cycles controlled third-order eustatic sequences in the Mesozoic and Paleozoic eustatic sequences (Boulila et al., 2011; Crampton et al., 2018; Zhong et al., 2018). In particular, Zhong et al. (2018) calibrated the Middle Ordovician time scale and demonstrated the prevailing influence of 1.2-Myr obliquity cycles from the Middle

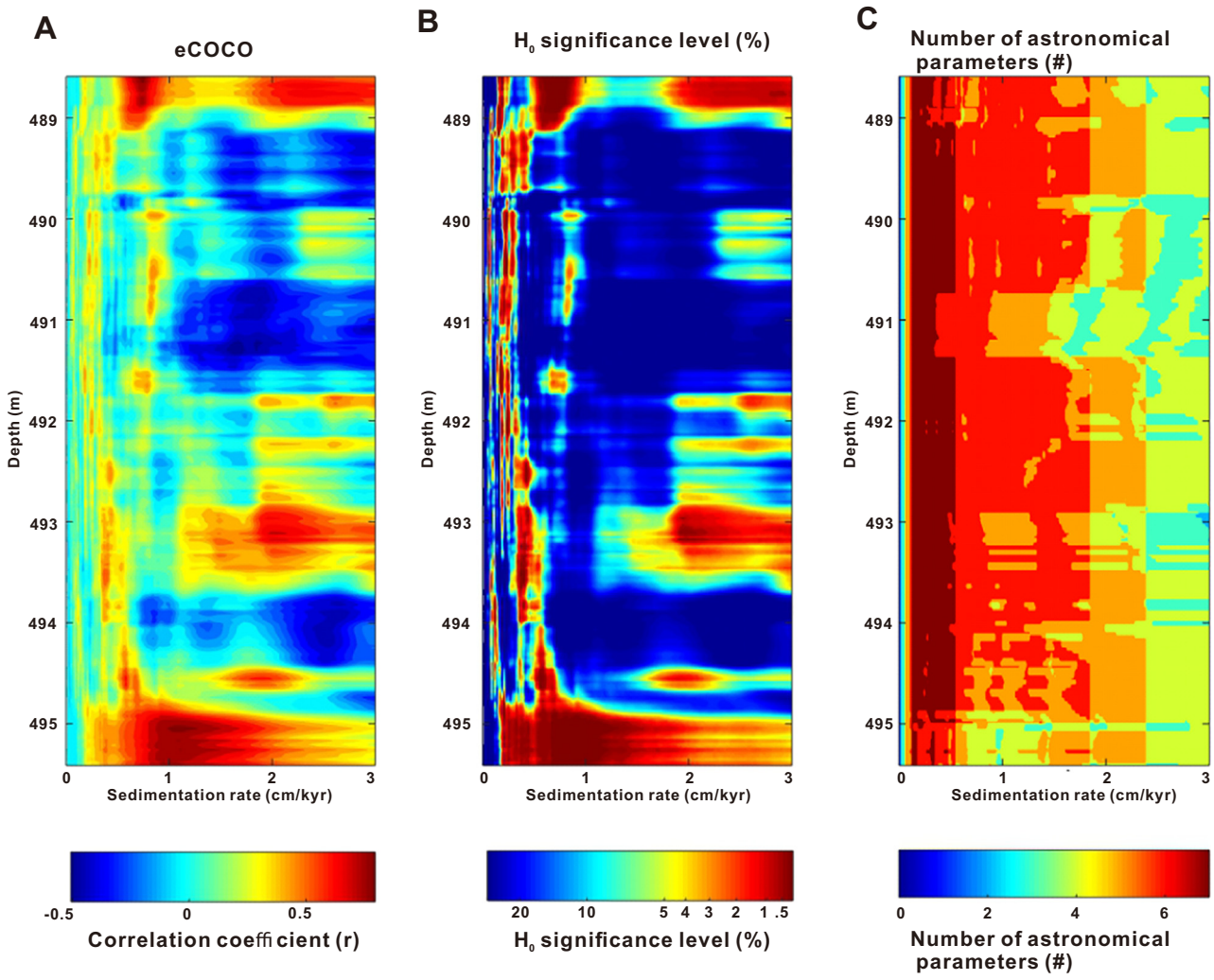

Fig. 6. eCOCO sedimentation rate map of the Fe^{3+} series in the studied section. A. Evolutionary correlation coefficient. B. Evolutionary H_0 significance level. C. Evolutionary map of the number of contributing astronomical parameters. The sliding window size is 2 m; the number of Monte Carlo simulations is 2000. Sedimentation rate from 0 to 3 cm/kyr with a step of 0.01 cm/kyr.

Ordovician through towards the Late Ordovician (Zhong et al., 2018). The results of this study reveal four ~1.2-Myr obliquity cycles, suggesting a prolonged influence of 1.2-Myr obliquity cycle in the late Katian through Hirnantian. Assuming constant tectonic subsidence and a bathymetric model, a case study on the margin of Gondwana (Central Anti-Atlas, southern Morocco) converted changes in facies-based water depths into a eustatic sea-level curve via a high-frequency-sequential back-stripping approach (Loi et al., 2010) (Fig. 8). Rather than the ~1.2-Myr cycles, it was believed that the ~2.4-Myr astronomical cycles were driving the third-order sequence development in the Late Ordovician (Loi et al., 2010), and there were two major sea-level falls (G1, G2) tied to the mid-late Hirnantian (Fig. 8). Both ~2.4-Myr and ~1.2-Myr cycles are considered as long-period modulation cycles. The ~1.2-Myr periods originate from inclination variation of Earth and Mars, with interfering terms of ~41-kyr (p + s3) and ~39-kyr (p + s4), where p is the Earth's axial precession frequency; s3 and s4 represent the obliquity modulation (Laskar et al., 2004). The ~2.4-Myr periods originate from the interactions between the orbital perihelia of Mars and Earth, with interfering terms of and ~95-kyr (g4–g5) and ~99-kyr (g3–g5) (Laskar et al., 2004). Moreover, Raymo et al. (2011) and Stocchi et al. (2013) demonstrated that the relationship between ice-sheet growth and relative sea-level fall is less linear than thought previously. Stocchi et al. (2013) studied on the onset of the Antarctic glaciation at the Eocene-Oligocene transition, and their results indicated that the sea-level change of near-field (high latitude regions) showing a substantial deviation from the global eustatic signal due to crustal deformation and gravitational perturbations. In the same way, the sea-level fall documented by Loi et al. (2010) along the margin of Gondwana (150 m) may significantly underestimate the Late Ordovician eustatic variations and should be considered as a lower end-member (Stocchi et al., 2013). Therefore, the sedimentary record in this study from a low latitude region is a better alternative to represent the genuine global eustatic change.

Another widely adopted third-order eustatic cycles that associated with the contemporaneous sea-level curve was proposed by Haq and Schutter (2008) that was modified by Ogg et al. (2016) following the advice of Bilal Haq. Within the studied interval, there are six major sea-level oscillations (Q1 to Q6) from the late Katian (448 Ma) to the end of Hirnantian (443.8 Ma) (Fig. 8), including two condensed sections (very thin stratigraphic units in the sedimentary sequence consisting of semi-pelagic or pelagic sediments that deposited at a sedimentation rate < 1 cm/kyr) Q1 and Q5 (Fig. 8). The sedimentation rate of the upper Katian through Hirnantian organic-rich shales is ~0.19 cm/kyr; hence, the entire section could be considered as one large condensed section unit with four major eustatic oscillations. The varying sea-level amplitudes of Q1 to Q4 are between 25 and 50 m, and > 75 m for Q5 and Q6 (Haq and Schutter, 2008; Ogg et al., 2016) (Fig. 8). Q1 and Q4 are very similar to O1 and O3, respectively (Fig. 8. Noted that the sea-level

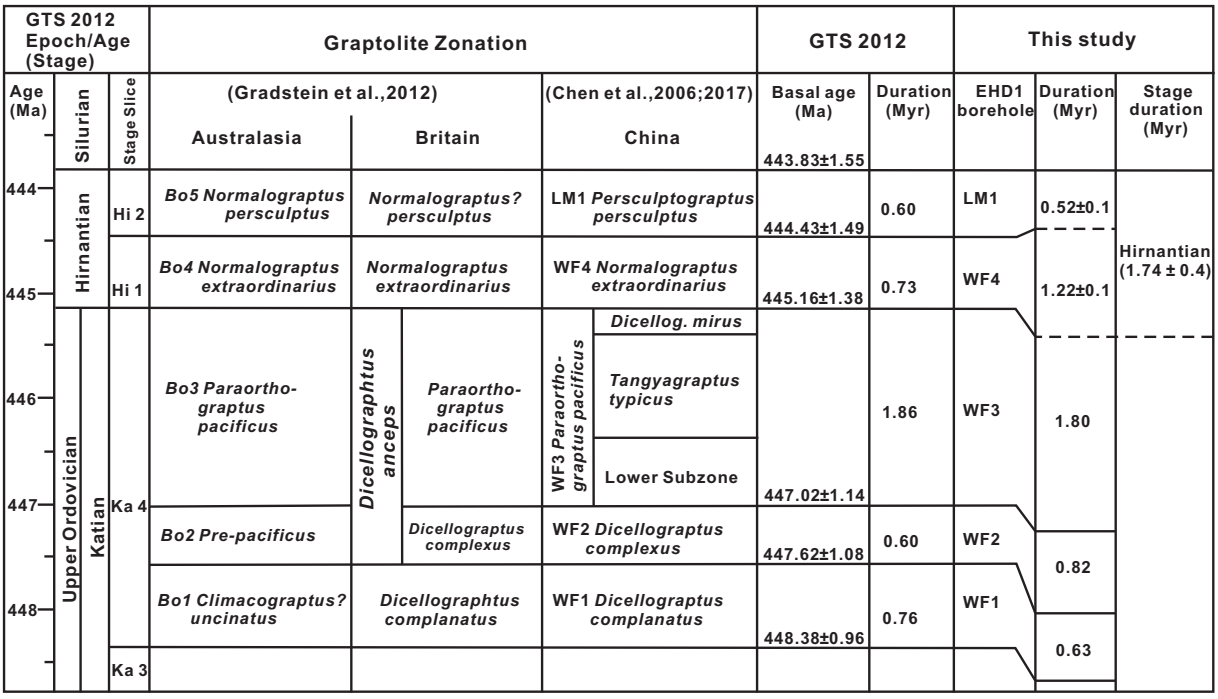

Fig. 7. Comparison between the Late Ordovician time scales of GTS2012 (Cooper, 2012) and the floating astronomical time scale established in this study. Dashed lines indicate uncertainty in boundary positions.

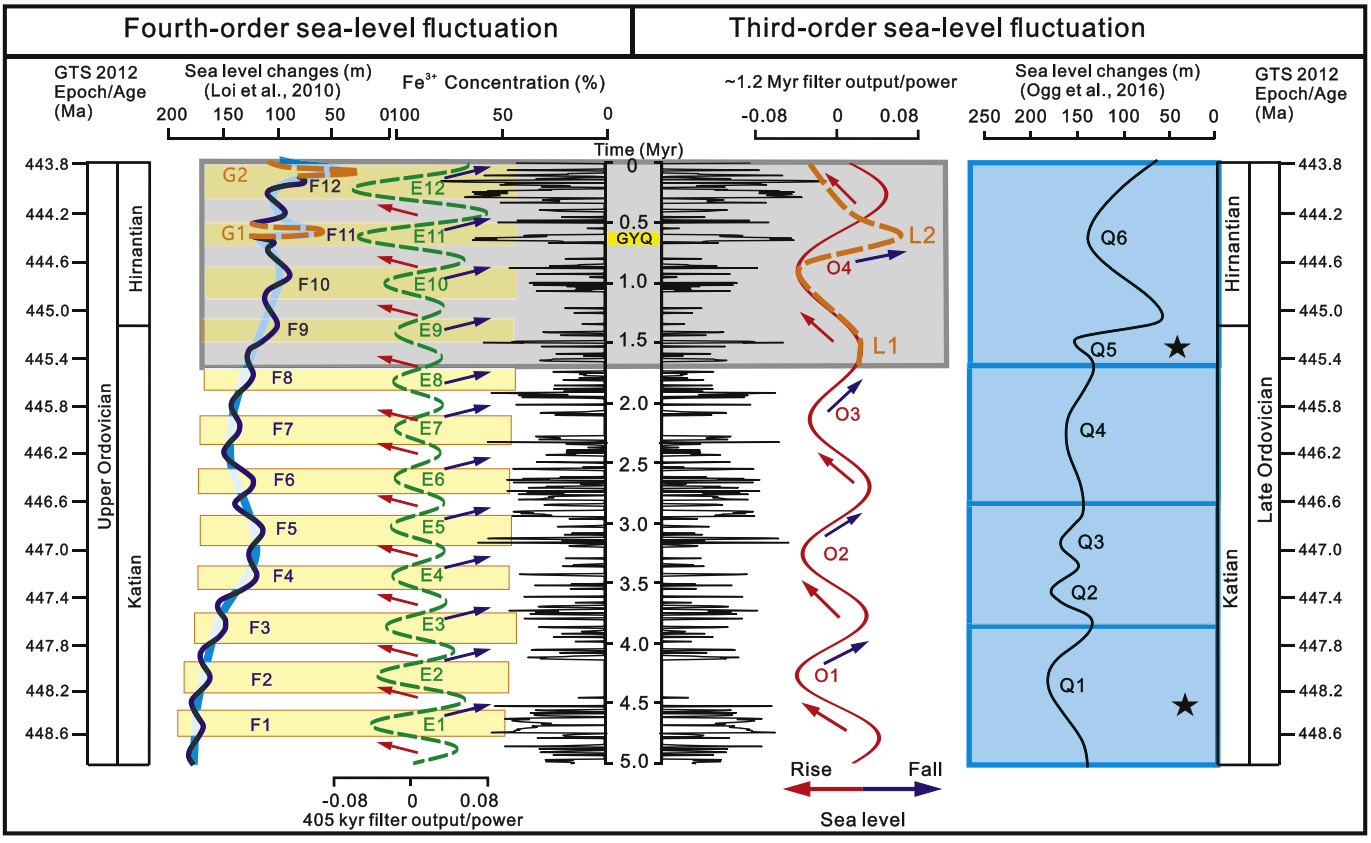

Fig. 8. Orbital forcing and sea-level fluctuations. E represents 405-kyr eccentricity, O represents 1.2-Myr obliquity. Q1 to Q6 represent the major third-order sea-level fluctuations (Ogg et al., 2016 following the advice of Bilal Haq); Asterisks represent condensed section (Haq and Schutter, 2008). F1 to F12 and line in dark blue represent 12 significant fourth-order sea-level fluctuations; Line in light blue represents third-order sea-level fluctuations. G1 and G2 represent dramatic sea-level falls within the Hirnantian (Loi et al., 2010). L1 and L2 represent reexamined third-order eustatic changes in the Hirnantian; GYQ = Guanyinqiao Bed; Area with shaded gray color represent the inferred duration of the Hirnantian in this study. (For interpretation of the references to color in this figure legend, the reader is referred to the web version of this article.)

rise or fall is an indicative interpretation of the timing of the eustatic change, quantitative estimation of the amplitude of sea-level variation is not attempted in this study). O2 is comparable with Q2 and Q3 that two smaller cycles are recognized within the grand cycle O2. The major discordance is within the duration of Hirnantian. Nevertheless, a consensus has been reached that there are two major sea-level falls associated with two third-order eustatic sequences within the Hirnantian (Armstrong and Coe, 1997; Haq and Schutter, 2008; Loi et al., 2010; Finnegan et al., 2011; Ghienne et al., 2014; Al-Husseini, 2016), although the timing of these two cycles varies in individual study. Furthermore, the mechanism or change in the carbon cycle that drove the Hirnantian glaciation is still under debate. Hypotheses include enhanced silicate weathering (Kump et al., 1999); changes in the balance of the carbon cycle (Brenchley et al., 2003); increased planetary albedo caused by high rates of volcanism (Buggisch et al., 2010) and improved efficiency of the biological pump (Shen et al., 2018), or it could be a combined effect with all those factors contributing. The scenario of eustatic sequences in the Hirnantian is much more complicated than it was in the late Katian. Thus, a close linkage (similar to O1, O3 and Q1, Q4) between the astronomical signals and third-order eustatic sequences is not expected in the Hirnantian stage. The pattern of the Hirnantian sea-level curve was reexamined with cautiousness. The Guanyinqiao Bed represents the glacial maximum, and it should be tied to the second major sea-level fall in the Hirnantian (Fig. 8) whereas the first sea-level fall was tied to the interval during the deposition of black calcareous mudstone that shows peaks in Fe^{3+} series in the early Hirnantian. The timing of the first sea-level fall in herein is consistent with the previous studies (Haq and Schutter, 2008; Ghienne et al., 2014; Al-Husseini, 2016). In that case, the third-order eustatic fluctuation in the Hirnantian should be more similar to the pattern and structure of L1 and L2 oscillations (Fig. 8).

5.3. Orbitally-forced paleoenvironmental changes and fourth-order eustatic sequences

Precession and eccentricity-dominated patterns of climate change are the most pronounced in the middle to low latitudes, whereas the climatic effects of obliquity oscillation are the most pronounced in (but not confined to) polar regions (Williams, 1991; Laskar et al., 2004). The low paleolatitude of the Yangtze area reveals a strong eccentricity dominated pattern, as the Fe^{3+} profile exhibits approximately twelve 405-kyr long-eccentricity cycles. This strong eccentricity pattern could originate from the precession index forcing of sedimentation, which led to 'rectification' of the forcing by the depositional process that transferred the eccentricity-forced amplitude modulations of the precession index into a directly observed signal (e.g., Ripepe and Fischer, 1991; Huang et al., 2010).

A case study of Cretaceous strata suggests that the 405-kyr long-eccentricity cycles have been one of the critical factors controlling the fourth-order sea-level changes (Gale et al., 2002). Their results raise a question whether a similar mechanism was present in the Late Ordovician? Twelve 405-kyr eccentricity cycles in this study were compared to the fourth-order sea-level fluctuations illustrated by Loi et al. (2010). For the same period, twelve sea-level fluctuations (F1 to F12) with amplitudes of ten to several tens of meters were recognized by Loi et al. (2010). Unlike the third-order eustatic sequences, E1 to E12 cycles of this study match adequately with the 'F' cycles of Loi et al. (2010), implying persistent 405-kyr eccentricity forced sea-level fluctuations from the late Katian through Hirnantian. The amplitudes of these twelve sea-level fluctuations were estimated to be within the range of ~10–25 m (Haq and Schutter, 2008; Loi et al., 2010). Sea-level fluctuations with amplitudes within 10 m may be ascribable to a range of mechanisms such as groundwater storage and lake-level variations, as well as changes in ocean temperature and consequent thermal expansion/contraction (e.g., Revelle, 1990). Amplitudes of sea-level changes exceeding 10 m most likely point to glacioeustatic control (Loi et al., 2010), indicating that twelve orbitally controlled sea-level fluctuations E1 to E12 were most likely glacioeustatic. Besides, Pohl et al. (2016a) used an Earth system model with an innovative coupling method between the ocean, atmosphere, and land ice accounting for climate and ice-sheet feedback processes to examine the evolution the Ordovician ice sheet. Their results suggested that the emergence of the ice sheet happened in two discrete phases, where the first ice-sheet growth possibly occurred as early as the Middle Ordovician Darriwilian, and the land ice growth was controlled by ablation rather than accumulation (Pohl et al., 2016a). As such, E1 to E12 may represent the minor extent of ice-sheet shrinkage and expansion that occurred between two discrete phases of ice-sheet development, supporting the hypothesis that a permanent ice sheet occupied the paleo-South Pole (present-day North Africa) throughout the Late Ordovician.

5.4. Orbitally-driven organic-rich shale development

The generation of OM has been a long-term debate, with two existing models for the generation of OM-enriched shales: the paleoproductivity model (e.g., Pedersen and Calvert, 1990; Sageman et al., 2003) and the preservation model (e.g., Arthur et al., 1998; Mort et al., 2007).

During the deposition of the upper Katian through Hirnantian organic-rich shales, the low-latitude Upper Yangtze area was surrounded by paleo-uplifts of carbonate platforms and in communication with the Qinling ocean through relatively narrow straits. The center and inner part of the Upper Yangtze area (e.g. Fuling and Changning area) were enclosed, semi-restricted, low-energy and anoxic basin environment that ensured suitable conditions for OM preservation (Yan et al., 2009; Ma et al., 2016; Lu et al., 2017) (Fig. 1) whereas the study area was located close to the open ocean (Fig. 1A). A better ventilation condition between the study area and open ocean would lead to high sensitivity to the signal of orbitally-forced eustatic fluctuations. The observed strong obliquity signals overprinted on the long-term trend of Cu/Ti, Ni/Ti series could also be elucidated by an obliquity-induced upwelling model (Fang et al., 2018). Low obliquity would reduce the total annual solar radiation during high-latitude summers, thus leading to reduced melting of the previous winter's snow and ice. This would have promoted ice-sheet growth in the high southern latitudes. In contrast, increased obliquity led to higher insolation gradients and loss of ice. Changes in obliquity would also greatly influence the thermohaline circulation intensity (Beauchamp and Baud, 2002). An upwelling zone perhaps developed along the epicontinental slope of the studied area. During a period of low obliquity, glacial inception would initiate an enhanced thermohaline circulation that produced upwelling zones, and thermohaline circulation transported glaciation-induced upwelling supplied nutrient-laden water from high latitude regions to the surface water of low-latitude Upper Yangtze area. Whereas during the period of high obliquity, elevated sea level tends to weaken thermohaline circulation and therefore intensify the stratification of the water column during glacial minima (Beauchamp and Baud, 2002). Pohl et al. (2016b) used a general circulation model with coupled components for ocean and atmosphere to examine the temperature and ocean-circulation in the Ordovician period. Their results also showed that lower temperature induced more active and vigorous ocean circulations between the high-latitude and low-latitude regions.

On the other hand, the paleoenvironment was relatively warm and humid even during the cooling period, as South China was located near the paleo-equator during the late Katian through Hirnantian. A lower eustatic sea level during a period of low obliquity led to greater exposure of land mass and elevation of Fe^3 content. Fe^{3+} maxima were interpreted as intervals of increased terrigenous dust flux or river runoff, and not as intervals of increased carbonate dissolution caused by poor deep-water ventilation, based on the covariance of Fe^{3+} and Ti, and the lack of covariance of Fe^{3+} and Mg (Fig. 9). Eventually, higher input of terrestrial nutrient was introduced into the water column and

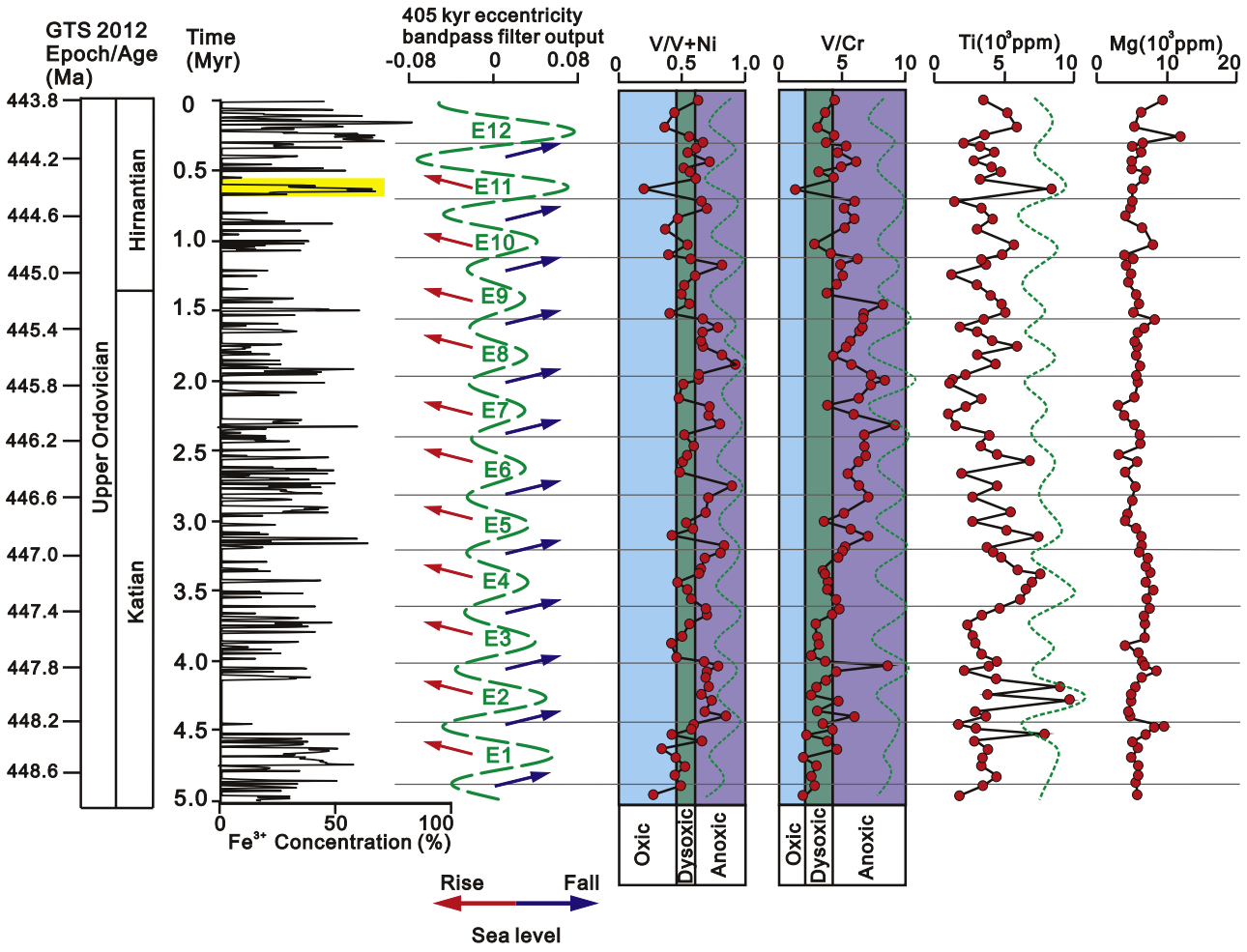

Fig. 9. 405-kyr tuned Fe^{3+} series, redox proxies (V/V + Ni and V/Cr) Ti and Mg concentration series with 405-kyr filtered outputs. The redox proxies and terrigenous input reflect the cyclic variations and the linkage between cycles and fourth-order eustatic changes. There is no close link between the Mg profile and 405-kyr tuned Fe^{3+} series. The area shaded with yellow represent the GYQ Bed. (For interpretation of the references to color in this figure legend, the reader is referred to the web version of this article.)

further enhance the primary productivity. However, the nutrient elevation through terrestrial input might be trivial comparing to the effect of upwelling due to a general low sedimentation rate throughout the studied section. It also draws the attention that the Cu/Ti, Ni/Ti, and TOC are yielding high values at the first dramatic sea-level fall (L1) during the late Katian-Hirnantian transition, suggesting that the amplitude of sea-level fall was not as much as previously expected by Haq and Schutter (2008), and the thermohaline circulation was still active during the first lowstand (Fig. 10). In the opposite, a higher amplitude of sea-level fall during the deposition of Guanyinqiao Bed thoroughly sequestered the Upper Yangtze area from the open ocean. The thermohaline circulation and upwelling were hampered throughout the glacial maximum. The upwelling rejuvenated after the termination of the Hirnantian glaciation, while the melting ice-sheet triggered a significant global marine transgression. To sum up, this study suggests that enhanced paleoproductivity though upwelling and terrestrial input also play essential roles in OM enrichment in the upper Katian through Hirnantian organic-rich shales.

6. Conclusions

In this work, we conducted a cyclostratigraphic analysis of high-resolution Fe^{3+} data from the Upper Ordovician Wufeng Formation and the lowermost Longmaxi Formation in the Yichang area, South China. In this low-latitude continuous marine sedimentary record, there is substantive evidence of Milankovitch signals. An integrated 405-kyr-tuned floating astronomical time scale of the late Katian through Hirnantian was constructed. There is a general agreement between the cyclostratigraphic age and radiometric dates in GTS2012. The durations of contemporaneous graptolite zones were re-evaluated from the late Katian through Hirnantian, and the duration of WF4 was ~0.5 Myr than previously thought.

Spectral analysis of the Fe^{3+} series revealed the presence of ~1.2-Myr and ~405-kyr periodicities related to long-period obliquity and long eccentricity, respectively. Close links between the orbital periodicities and third- and fourth-order eustatic changes were successfully established. This study proposes that the studied interval is a condensed section composed of four major third-order cycles driven by ~1.2-Myr long obliquity. Within each major cycle, ~3–4 fourth-order cycles were recognized, and are associated with ice-sheet expansion and shrinkage driven by 405-kyr eccentricity, supporting the hypothesis of continuous pre-Hirnantian ice-sheet development.

Finally, this work demonstrates that strong ~1.2-Myr obliquity signals can be recognized in Cu/Ti, Ni/Ti, and TOC data, and this is likely a result of obliquity-mediated upwelling changes. Besides favorable preservation conditions controlled by basin geometry, obliquity-forced nutrient availability was probably one of the key factors controlling OM enrichment in the upper Katian through Hirnantian organic-rich shale, as enhanced cooling triggered ice-sheet expansion and concurrent sea-level fall that triggered higher thermohaline circulation

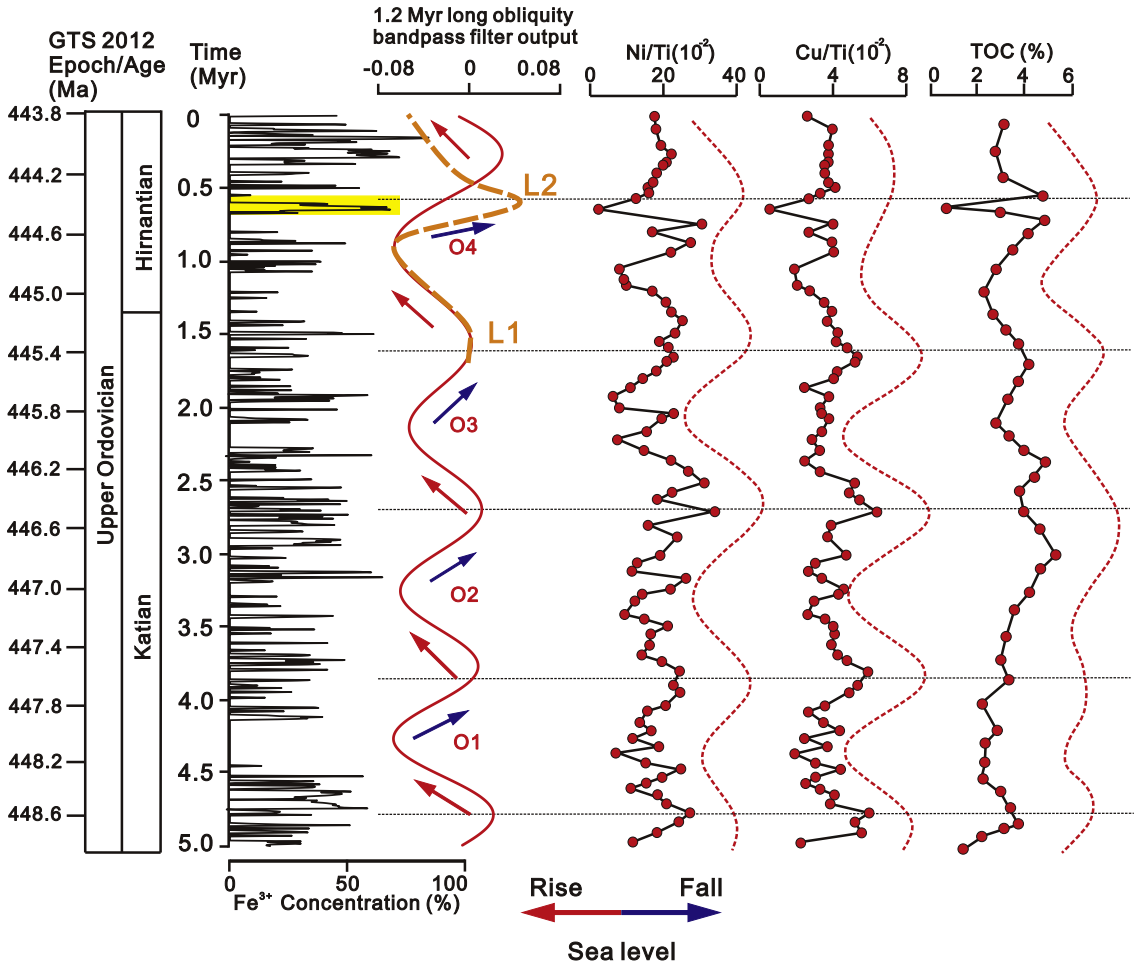

Fig. 10. Raw data of Fe^{3+} series, paleoproductivity proxies (Ni/Ti and Cu/Ti) and TOC concentration. 1.2-Myr long obliquity filtered output of paleoproductivity proxies and TOC concentration reflect the cyclic variations and the linkage between cycles and third-order eustatic changes. The area shaded with yellow represent the GYQ Bed. (For interpretation of the references to color in this figure legend, the reader is referred to the web version of this article.)

intensity and enhanced paleoproductivity through upwelling and weathering. In contrast, warming intervals led to ice-sheet shrinkage and concurrent deepening characterized by water column stratification and reduced nutrient supply.

Acknowledgments

This research was supported by the National Natural Science Foundation of China (41690131; 41772029; 41728004) and the Program of Introducing Talents of Discipline to Universities (No. B14031), Natural Science Foundation for Distinguished Young Scholars of Hubei Province of China (2016CFA051) and the Fundamental Research Funds for the Central Universities, China University of Geosciences, Wuhan (No. CUGCJ1703, CUGQYZX1705). We appreciate the data support (including well log and core data) from the Research Institute of Jianghan Oil Filed, SINOPEC.

References

Achab, A., Paris, F., 2007. The Ordovician chitinozoan biodiversification and its leading factors. Palaeogeogr. Palaeoclimatol. Palaeoecol. 245, 5–19.
Ainsaar, L., Meidla, T., Martma, T., 1999. Evidence for a wide-spread carbon isotopic event associated with late Middle Ordovician sedimentation and faunal changes in Estonia. Geol. Mag. 136, 49–62.
Ainsaar, L., Meidla, T., Martma, T., 2004. The middle Caradoc facies and faunal turnover in the late Ordovician Baltoscandian palaeobasin. Palaeogeogr. Palaeoclimatol. Palaeoecol. 210, 119–133.
Algeo, T.J., Marenco, P.J., Saltzman, M.R., 2016. Co-evolution of oceans, climates, and the biosphere during the Ordovician Revolution: a review. Palaeogeogr. Palaeoclimatol. Palaeoecol. 458, 1–11.
Al-Husseini, M.I., 2016. Late Ordovician-Early Silurian orbital-forcing of glacio-eustacy. http://www.orbitalscale.net/Projects/study/AlHusseini%202016%20Orbiton%2031.pdf, Accessed date: 2 February 2019.
Armstrong, H.A., Coe, A.L., 1997. Deep-sea sediments record the geophysiology of the late Ordovician glaciation. J. Geol. Soc. 154 (6), 929–934.
Arthur, M.A., Dean, W.E., Laarkamp, K., 1998. Organic carbon accumulation and preservation in surface sediments on the Peru margin. Chem. Geol. 152 (3), 273–286.
Beauchamp, B., Baud, A., 2002. Growth and demise of Permian biogenic chert along northwest Pangea: evidence for End-Permian collapse of thermohaline circulation. Palaeogeogr. Palaeoclimatol. Palaeoecol. 184, 37–63.
Berger, A., Loutre, M.F., 1994. Astronomical forcing through geological time. In: De Boer, P.L., Smith, D.G. (Eds.), Orbital Forcing and Cyclic Sequences. Blackwell Scientific Publications, Oxford, pp. 15–24.
Berger, A., Loutre, M.F., Laskar, J., 1992. Stability of the astronomical frequencies over the Earth's history for paleoclimate studies. Science 255, 560–566.
Boulila, S., Galbrun, B., Miller, K.G., Pekar, S.F., Browning, J.V., Laskar, J., Wright, J.D., 2011. On the origin of Cenozoic and Mesozoic "third-order" eustatic sequences. Earth Sci. Rev. 109 (3), 94–112.
Bourahrouh, A., Paris, F., Elaouad-Debbaj, Z., 2004. Biostratigraphy, biodiversity and palaeoenvironments of the chitinozoans and associated palynomorphs from the Upper Ordovician of the Central Anti-Atlas, Morocco. Rev. Palaeobot. Palynol. 130, 17–40.
Brenchley, P.J., Marshall, J.D., Carden, G.A.F., Robertson, D.B.R., Long, D.G.F., Meidla, T., Hints, T., Anderson, T.F., 1994. Bathymetric and isotopic evidence for a short-lived late Ordovician glaciation in a greenhouse period. Geology 22 (4), 295.
Brenchley, P.J., Cardem, G.A., Hints, L., Kaljo, D., Marshall, J.D., Martma, T., Meidla, T., Nõlvak, J., 2003. High-resolution stable isotope stratigraphy of Upper Ordovician sequences: constraints on the timing of bioevents and environmental changes associated with mass extinction and glaciation. Geol. Soc. Am. Bull. 115, 89–104.
Buggisch, W., Joachimski, M.M., Lehner, O., Bergström, S.M., Repetski, J.E., Webers, G.F., 2010. Did intense volcanism trigger the first Late Ordovician icehouse? Geology 38, 327–330.

Calvert, S.E., Pedersen, T.F., 1993. Geochemistry of recent oxic and anoxic marine sediments: Implications for the geological record. Mar. Geol. 113 (1), 67–88.
Chen, X., Rong, J.Y., Li, Y., Boucot, A.J., 2004. Facies patterns and geography of the Yangtze region, South China, though the Ordovician and Silurian transition. Palaeogeogr. Palaeoclimatol. Palaeoecol. 20, 353–372.
Chen, X., Rong, J.Y., Fan, J.X., Zhan, R.B., Mitchell, C.E., Harper, D.A.T., Melchin, M.J., Peng, P.A., Finney, S.C., Wang, X.F., 2006. The global boundary stratotype section and point (GSSP) for the base of the Hirnantian Stage (the uppermost of the Ordovician System). Episodes 29, 183–196.
Chen, X., Bergström, S.M., Zhang, Y.D., Wang, Z.H., 2013. A regional tectonic event of Katian (Late Ordovician) age across three major blocks of China. Chin. Sci. Bull. 58 (34), 59–65.
Chen, X., Fan, J.X., Chen, Q., Tang, L., Hou, X.D., 2014. Toward a stepwise Kwangsian Orogeny. Sci. China Earth Sci. 57 (3), 379–387.
Chen, C., Mu, C.L., Zhou, K.K., Liang, W., Ge, X.Y., Wang, X.P., Wang, Q.Y., Zheng, B.S., 2016. The geochemical characteristics and factors controlling the organic matter accumulation of the late Ordovician-Early Silurian black shale in the Upper Yangtze Basin, South China. Mar. Pet. Geol. 76, 159–175.
Chen, X., Fan, J.X., Wang, W.H., Wang, H.Y., Nie, H.K., Shi, X.W., Wen, Z.D., Chen, D.Y., Li, W.J., 2017. Stage-progressive distribution pattern of the Longmaxi black graptolitic shales from Guizhou to Chongqing, Central China. Sci. China Earth Sci. 60 (6), 1133–1146.
Chen, X., Chen, Q., Zhen, Y.Y., Wang, H.Y., Zhang, L.N., Zhang, J.P., Wang, W.H., Xiao, Z.H., 2018. Circumjacent distribution pattern of the Lungmachian graptolitic black shale (early Silurian) on the Yichang Uplift and its peripheral region. Sci. China Earth Sci. 61, 1195–1203.
Cooper, R.A., 2012. The Ordovician period. In: Gradstein, F.M., Ogg, J.G., Schmitz, M.D., Ogg, G.M. (Eds.), The Geologic Time Scale 2012, 1st ed. Elsevier, Amsterdam, pp. 504.
Crampton, J.S., Meyers, S.R., Cooper, R.A., Sadler, P.M., Foote, M., Harte, D., 2018. Pacing of Paleozoic macroevolutionary rates by Milankovitch grand cycles. PNAS 115 (22), 5685–5691.
Dahl, T.W., Ruhl, M., Hammarlund, E.U., Canfield, D.E., Rosing, M.T., Bjerrum, C.J., 2013. Tracing euxinia by molybdenum concentrations in sediments using handheld X-ray fluorescence spectroscopy (HHXRF). Chem. Geol. 360 (1), 241–251.
De Vleeschouwer, D., Whalen, M.T., Day, J.E., Claeys, P., 2012. Cyclostratigraphic calibration of the Frasnian (Late Devonian) time scale (western Alberta, Canada). Geol. Soc. Am. Bull. 124, 928–942.
Delabroye, A., Vecoli, M., 2010. The end-Ordovician glaciation and the Hirnantian Stage: A global review and questions about Late Ordovician event stratigraphy. Earth Sci. Rev. 98 (3–4), 269–282.
Elrick, M., Reardon, D., Labor, W., Martin, J., Desrochers, A., Pope, M., 2013. Orbital-scale climate change and glacioeustasy during the early Late Ordovician (pre-Hirnantian) determined from $\delta^{18}O$ values in marine apatite. Geology 41, 775–778.
Fan, J.X., Peng, P.A., Melchin, M.J., 2009. Carbon isotopes and event stratigraphy near the Ordovician–Silurian boundary, Yichang, South China. Palaeogeogr. Palaeoclimatol. Palaeoecol. 276, 160–169.
Fang, Q., Wu, H.C., Hinnov, L.A., Wang, X.L., Yang, T.S., Li, H.Y., Zhang, S.H., 2016. A record of astronomically forced climate change in a Late Ordovician (Sandbian) deep marine sequence, Ordos Basin, North China. Sediment. Geol. 341, 163–174.
Fang, Q., Wu, H.C., Hinnov, L.A., Wang, Q.T., Wang, X.L., Yang, T.S., Li, H.Y., Zhang, S.H., 2018. Abiotic and biotic responses to Milanvovitch-forced megamonsoon and glacial cycles recorded in South China at the end of the Late Paleozoic Ice Age. Glob. Planet. Chang. 163, 97–108.
Finnegan, S., Bergmann, K., Eiler, J.M., Jones, D.S., Fike, D.A., Eisenman, I., Hughes, N.C., Tripati, A.K., Fischer, W.W., 2011. The magnitude and duration of Late Ordovician-Early Silurian glaciation. Science 331 (6019), 903.
Gale, A.S., Hardenbol, J., Hathway, B., Kennedy, W.J., Young, J.R., Phansalkar, V., 2002. Global correlation of Cenomanian (Upper Cretaceous) sequences: evidence for Milankovitch control on sea level. Geology 30 (4), 291–294.
Ghavidel-Syooki, M., 2017. Stratigraphic evidence for Hirnantian glaciation in the Alborz Mountain Ranges, northeastern Iran. Palaeogeogr. Palaeoclimatol. Palaeoecol. 485, 879–898.
Ghienne, J.F., Desrochers, A., Vandenbroucke, Thijs R.A., Achab, A., Asselin, E., Dabard, M.-P., Farley, C., Loi, A., Paris, F., Wickson, S., Veizer, J., 2014. A Cenozoic-style scenario for the end-Ordovician glaciation. Nat. Commun. 5, 4485.
Ghil, M., Allen, M.R., Dettinger, M.D., Ide, K., Kondra-shov, D., Mann, M.E., Robertson, A.W., Saunders, A., Tian, Y., Varadi, F., Yiou, P., 2002. Advanced spectral methods for climatic time series. Rev. Geophys. 40 (1), 3-1–3-41.
Gradstein, F.M., Ogg, J.G., Schmitz, M.D., Ogg, G.M., 2012. The Geologic Time Scale 2012, 1st ed. Elsevier, Amsterdam, pp. 491–513.
Hamoumi, N., 1999. Upper Ordovician glaciation spreading and its sedimentary record in Moroccan North Gondwana margin. Acta Univ. Carol. Geol. 43, 111–114.
Haq, B.U., Schutter, S.R., 2008. A chronology of Paleozoic sea-level changes. Science 322, 64–68.
Hatch, J.R., Leventhal, J.S., 1992. Relationship between inferred redox potential of the depositional environment and geochemistry of the Upper Pennsylvanian (Missourian) stark shale member of the Dennis limestone, Wabaunsee country, Kansas, USA. Chem. Geol. 99, 65–82.
Higgins, J.A., Schrag, D.P., 2010. Constraining magnesium cycling in marine sediments using magnesium isotopes. Geochim. Cosmochim. Acta 74 (17), 5039–5053.
Hinnov, L.A., Diecchio, R.J., 2016. Milankovitch cycles in the Juniata Formation, Late Ordovician, Central Appalachian Basin, USA. Stratigraphy 12, 287–296.
Huang, C.J., Hesselbo, S.P., Hinnov, L., 2010. Astrochronology of the Late Jurassic Kimmeridge Clay (Dorset, England) and implications for Earth system processes. Earth Planet. Sci. Lett. 289 (12), 242–255.
Huang, C.J., Deng, S.H., Dong, S.S., Hinnov, L., Zhang, R., Wang, Z.X., Lu, Y.Z., Li, X., 2016. Astronomically forced cyclicity in the Late Ordovician-Early Silurian, Sichuan Basin, China. In: GSA Annual Meeting in Denver, Colorado, USA.
Huang, B.C., Yan, Y.G., Piper, J.D.A., Zhang, D.H., Yi, Z.Y., Yu, S., Zhou, T.H., 2018. Paleomagnetic constraints on the paleogeography of the East Asian blocks during Late Paleozoic and Early Mesozoic times. Earth Sci. Rev. 186 (5), 8–36.
Imbrie, J., Hays, J.D., Martinson, D.G., McIntyre, A., Mix, A.C., Morely, J.J., Pisias, N.G., Prell, W.L., Shackleton, N.G., 1984. The orbital theory of Pleistocene climate: support from a revised chronology of the marine $\delta^{18}O$ record. In: Berger, A.L., Imbrie, J., Hays, J.D., Kukla, G., Saltzman, B. (Eds.), Milankovitch and Climate, Part 1. D. Reidel Publishing Co., Dordrecht, pp. 269–305.
Jones, B., Manning, D.A.C., 1994. Comparison of geochemical indices used for the interpretation of palaeoredox conditions in ancient mudstone. Chem. Geol. 111, 111–129.
Kuiper, K.F., Deino, A., Hilgen, F.J., Krijgsman, W., Renne, P.R., Wijbrans, J.R., 2008. Synchronizing rock clocks of Earth history. Science 320 (5875), 500–504.
Kump, L.R., Arthur, M.A., Patzkowsky, M., Gibbs, M., Pinkus, D., Sheehan, P., 1999. A weathering hypothesis for glaciation at high atmospheric pCO2 during the Late Ordovician. Palaeogeogr. Palaeoclimatol. Palaeoecol. 152, 173–187.
Laskar, J., Robutel, P., Joutel, F., Gastineau, M., Correia, A.C.M., Levrard, B., 2004. A long-term numerical solution for the insolation quantities of the Earth. Astron. Astrophys. 428, 261–285.
Lavoie, D., 1995. Late Ordovician high-energy temperate-water carbonate ramp, southern Quebec, Canada: implications for Late Ordovician oceanography. Sedimentology 42, 95–116.
Li, M.S., Kump, L.R., Hinnov, L.A., Mann, M.E., 2018. Tracking variable sedimentation rates and astronomical forcing in Phanerozoic proxy series with evolutionary correlation coefficient and hypothesis testing. Earth Planet. Sci. Lett. 501, 165–179.
Liu, Z.H., Algeo, T.J., Guo, X.S., Fan, J.X., Du, X.B., Lu, Y.C., 2017. Paleo-environmental cyclicity in the Early Silurian Yangtze Sea (South China): tectonic or glacio-eustatic control? Palaeogeogr. Palaeoclimatol. Palaeoecol. 466, 59–76.
Loi, A., 1993. Sedimentological-petrographical study and paleogeographical approach of the Upper Ordovician of the central southern Sardinia. European Journal of Mineralogy “Plinius” 9, 81–86.
Loi, A., Ghienne, J.F., Dabard, M.P., Paris, F., Botquelen, A., Christ, N., Elaouad-Debbaj, Z., Gorini, A., Vidal, M., Videt, B., 2010. The Late Ordovician glacio-eustatic record from a high-latitude storm-dominated shelf succession: the Bou Ingarf section (Antiatlas, Southern Morocco). Palaeogeogr. Palaeoclimatol. Palaeoecol. 296, 332–358.
Long, D.G., 2007. Tempestite frequency curves: a key to Late Ordovician and Early Silurian subsidence, sea-level change, and orbital forcing in the Anticosti foreland basin, Quebec, Canada. Can. J. Earth Sci. 44, 413–431.
Lu, Y.B., Ma, Y.Q., Wang, Y.X., Lu, Y.C., 2017. The sedimentary response to the major geological events and lithofacies characteristics of Wufeng-Longmaxi Formation in the Upper Yangtze Area. Earth Sci. 42 (7), 1169–1184 (in Chinese with English abstract).
Ma, Y.Q., Fan, M.J., Lu, Y.C., Guo, X.S., Hu, H.Y., Chen, L., Wang, C., Liu, X.C., 2016. Geochemistry and sedimentology of the lower Silurian Longmaxi mudstone in southwestern China: implications for depositional controls on organic matter accumulation. Mar. Pet. Geol. 75, 291–309.
Malinverno, A., Erba, E., Herbert, T.D., 2010. Orbital tuning as an inverse problem: chronology of the early Aptian oceanic anoxic event 1a (Selli Level) in the Cismon APTICORE. Paleoceanography 25, PA2203.
Mann, M.E., Lees, J.M., 1996. Robust estimation of background noise and signal detection in climatic time series. Clim. Chang. 33, 409–445.
Metcalfe, I., 1994. Late Palaeozoic and Mesozoic palaeogeography of Eastern Pangaea and Tethys. Global Environments and Resources 17, 97–111.
Mort, H., Jacquat, O., Adatte, T., Steinmann, P., Föllmi, K., Matera, V., Berner, Z., Stüben, D., 2007. The Cenomanian/Turonian anoxic event at the Bonarelli Level in Italy and Spain: enhanced productivity and/or better preservation. Cretac. Res. 28 (4), 597–612.
Nameroff, T.J., Garant, R.J., Albert, M.B., 2004. Adoption of green chemistry: an analysis based on US patents. Res. Policy 33 (6), 959–974.
Ogg, J.G., Ogg, G., Gradstein, F.M., 2016. A Concise Geologic Time Scales 2016, 1st ed. Elsevier, Amsterdam, pp. 234–240.
Paillard, D., Labeyrie, L., Yiou, P., 1996. Macintosh program performs time-series analysis. Eos AGU 77, 379.
Pas, D., Hinnov, L., Day, J.E., Kodama, K., Sinnesael, M., Liu, W., 2018. Cyclostratigraphic calibration of the Famennian stage (Late Devonian, Illinois Basin, USA). Earth Planet. Sci. Lett. 488, 102–114.
Pedersen, T.F., Calvert, S.E., 1990. Anoxia vs. productivity: what controls the formation of organic-carbon-rich sediments and sedimentary rocks. AAPG Bull. 74 (4), 454–466.
Pohl, A., Donnadieu, Y., Le Hir, G., Ladant, J.B., Dumas, C., Alvarez-Solas, J., Vandenbroucke, T.R.A., 2016a. Glacial onset predated Late Ordovician climate cooling. Paleoceanography 31 (6), 800–821.
Pohl, A., Nardin, E., Vandenbroucke, T.R.A., Donnadieu, Y., 2016b. High dependence of Ordovician ocean surface circulation on atmospheric CO_2 levels. Palaeogeogr. Palaeoclimatol. Palaeoecol. 458, 39–51.
Pope, M.C., Read, J.F., 1998. Ordovician meter-scale cycles: implications for climatic and eustatic fluctuations in the central Appalachians during a global greenhouse, non-glacial to glacial transition. Palaeogeogr. Palaeoclimatol. Palaeoecol. 138, 27–42.
Pope, M.C., Steffen, J.B., 2003. Widespread, prolongated late Middle to Late Ordovician upwelling in North America: a proxy record of glaciation? Geology 31, 63–66.
Raymo, M.E., Mitrovica, J.X.M., O'Leary, J., DeConto, R.M., Hearty, P.J., 2011. Departures from eustasy in Pliocene sea-level records. Nat. Geosci. 4 (5), 328–332.

Revelle, R.E., 1990. Sea Level Change. National Research Council, Studies in Geophysics. National Academy Press, Washington, pp. 234.
Rimmer, S.M., 2004. Geochemical paleoredox indicators in Devonian–Mississippian black shales, Central Appalachian Basin (USA). Chem. Geol. 206 (3–4), 373–391.
Ripepe, M., Fischer, A.G., 1991. Stratigraphic rhythms synthesized from orbital variations. In: Franseen, E.K., Watney, W.L., Kendall, C.G.St.C., Ross, W. (Eds.), Sedimentary Modeling: Computer Simulations and Methods for Improved Parameter Definition: Kansas Geological Survey, Bulletin. 233. pp. 335–344.
Rong, J.Y., Chen, X., Harper, D.A.T., 2002. The latest Ordovician Hirnantia Fauna (Brachiopoda) in time and space. Lethaia 35, 231–249.
Sageman, B.B., Murphy, A.E., Werne, J.P., Straeten, C.A.V., Hollander, D.J., Lyons, T.W., 2003. A tale of shales: the relative roles of production, decomposition, and dilution in the accumulation of organic-rich strata, Middle–Upper Devonian, Appalachian basin. Chem. Geol. 195 (1–4), 229–273.
Saltzman, M.R., Young, S.A., 2005. Long-lived glaciation in the Late Ordovician? Isotopic and sequence-stratigraphic evidence from western Laurentia. Bull. Geol. Soc. Am. 33, 109–112.
Schodlok, M.C., Whitbourn, L., Huntington, J., Coward, G.A., Connor, P., Mason, P., 2016. The HyLogger-3–a visible to shortwave and thermal infrared reflectance spectrometer system for drill core logging-function description. Aust. J. Earth Sci. 63, 929–940.
Shen, J.H., Pearson, A., Henkes, G.A., Zhang, Y.G., Chen, K.F., Li, D.D., Wankel, S.D., Finney, S.C., Shen, Y.N., 2018. Improved efficiency of the biological pump as a trigger for the Latte Ordovician glaciation. Nat. Geosci. 11, 510–514.
Stocchi, P., Escutia, C., Houben, A.J.P., Vermeersen, B.L.A., Bijl, P.K., Brinkhuis, H., DeConto, R.M., Galeotti, S., Passchier, S., Pollard, D., 2013. Relative sea-level rise around East Antarctica during Oligocene glaciation. Nat. Geosci. 6 (5), 380–384.
Strasser, A., Hilgen, F., Heckel, P., 2006. Cyclostratigraphy-concepts, definitions, and applications. Newsl. Stratigr. 42 (2), 75–114.
Sutcliffe, O.E., Dowdeswell, J.A., Whittington, R.J., Theron, J.N., Craig, J., 2000. Calibrating the Late Ordovician glaciation and mass extinction by the eccentricity cycles of Earth's orbit. Geology 28, 967–970.
Svensen, H.H., Hammer, Ø., Corfu, F., 2015. Astronomically forced cyclicity in the Upper Ordovician and U–Pb ages of interlayered tephra, Oslo region, Norway. Palaeogeogr. Palaeoclimatol. Palaeoecol. 418, 150–159.
Thomson, D.J., 1982. Spectrum estimation and harmonic analysis. Proc. IEEE 70, 1055–1096.
Tucker, R.D., Krogh, T.E., Ross, R.J.J., Williams, S.H., 1990. Time-scale calibration by high-precision U-Pb zircon dating of interstratified volcanic ashes in the Ordovician and lower Silurian stratotypes of Britain. Earth Planet. Sci. Lett. 100 (1–3), 51–58.
Waltham, D., 2015. Milankovitch period uncertainties and their impact on cyclostratigraphy. J. Sediment. Res. 85, 990–998.
Wang, H.Z., 1985. Atlas of the Palaeogeography of China. Cartographic Publishing House, Beijing, pp. 143 (in Chinese with English summary).
Westerhold, T., Röhl, U., Laskar, J., Raffi, I., Bowles, J., Lourens, L.J., Zachos, J.C., 2007. On the duration of magnetochrons c24r and c25n and the timing of early Eocene global warming events: implications from the ocean drilling program leg 208 walvis ridge depth transect. Paleoceanography 22 (2), PA2201.
Westerhold, T., Röhl, U., Raffi, I., Fornaciari, E., Monechi, S., Reale, V., Bowles, J., Evans, H.F., 2008. Astronomical calibration of the Paleocene time. Palaeogeogr. Palaeoclimatol. Palaeoecol. 257 (4), 377–403.
Williams, G.E., 1991. Milankovitch-band cyclicity in bedded halite deposits contemporaneous with Late Ordovician-Early Silurian glaciation, Canning Basin, Western Australia. Earth Planet. Sci. Lett. 103, 143–155.
Wu, H.C., Zhang, S.H., Hinnov, L.A., Jiang, G.Q., Feng, Q.L., Li, H.Y., Yang, T.S., 2013. Time-calibrated Milankovitch cycles for the Late Permian. Nat. Commun. 4, 2452.
Yan, D.T., Chen, D.Z., Wang, Q.C., Wang, J.G., Wang, Z.Z., 2009. Geochemical changes across the Ordovician-Silurian transition on the Yangtze platform, South China. Sci. China Ser. D Earth Sci. 52 (1), 38–54.
Zeng, W., Zhang, J., Ding, W., Zhao, S., Zhang, Y., Liu, Z., Jiu, K., 2013. Fracture development in Paleozoic shale of Chongqing area (South China). Part one: fracture characteristics and comparative analysis of main controlling factors. J. Asian Earth Sci. 75, 251–266.
Zhan, R.B., Liu, J.B., Percival, I.G., Jin, J.S., Li, G.P., 2010. Biodiversification of Late Ordovician Hirnantia fauna on the Upper Yangtze platform, South China. Science in China D: Earth Sciences 53, 1800–1810.
Zhong, Y.Y., Wu, H.C., Zhang, Y.D., Zhang, S.H., Yang, T.S., Li, H.Y., Cao, L.W., 2018. Astronomical calibration of the Middle Ordovician of the Yangtze Block, South China. Palaeogeogr. Palaeoclimatol. Palaeoecol. 505, 86–89.